



**HAL**  
open science

# Investigating the Shallow to Mid-Depth (>100–300 °C) Continental Crust Evolution with (U-Th)/He Thermochronology: A Review

Cécile Gautheron, Mathias Hueck, Sébastien Ternois, Beatrix Heller, Stéphane Schwartz, Philippe Sarda, Laurent Tassan-Got

## ► To cite this version:

Cécile Gautheron, Mathias Hueck, Sébastien Ternois, Beatrix Heller, Stéphane Schwartz, et al.. Investigating the Shallow to Mid-Depth (>100–300 °C) Continental Crust Evolution with (U-Th)/He Thermochronology: A Review. *Minerals*, 2022, 12 (5), pp.563. 10.3390/min12050563 . insu-03675552

**HAL Id: insu-03675552**

**<https://insu.hal.science/insu-03675552>**

Submitted on 23 May 2022

**HAL** is a multi-disciplinary open access archive for the deposit and dissemination of scientific research documents, whether they are published or not. The documents may come from teaching and research institutions in France or abroad, or from public or private research centers.

L'archive ouverte pluridisciplinaire **HAL**, est destinée au dépôt et à la diffusion de documents scientifiques de niveau recherche, publiés ou non, émanant des établissements d'enseignement et de recherche français ou étrangers, des laboratoires publics ou privés.



Distributed under a Creative Commons Attribution 4.0 International License

Review

# Investigating the Shallow to Mid-Depth (>100–300 °C) Continental Crust Evolution with (U-Th)/He Thermochronology: A Review

Cécile Gautheron <sup>1,\*</sup>, Mathias Hueck <sup>2</sup>, Sébastien Ternois <sup>3</sup>, Beatrix Heller <sup>1</sup>, Stéphane Schwartz <sup>4</sup>, Philippe Sarda <sup>1</sup> and Laurent Tassan-Got <sup>5</sup>

<sup>1</sup> Geosciences Paris Saclay (GEOPS), Université Paris Saclay, 91404 Orsay, France; bm.heller@gmx.de (B.H.); philippe.sarda@universite-paris-saclay.fr (P.S.)

<sup>2</sup> Instituto de Geociências, Universidade de São Paulo, São Paulo 38000, Brazil; mathiashueck@gmail.com

<sup>3</sup> Institut des Sciences de la Terre d'Orléans (ISTO), UMR 7327, Université d'Orléans, CNRS, BRGM, 45000 Orléans, France; seb.ter@hotmail.fr

<sup>4</sup> Université Grenoble Alpes, Université Savoie Mont Blanc, CNRS, IRD, Université Gustave Eiffel, ISTERre, 38000 Grenoble, France; stephane.schwartz@univ-grenoble-alpes.fr

<sup>5</sup> Laboratory of the Physics of the Two Infinities Irène Joliot-Curie (IJClab), Université Paris Saclay, 91404 Orsay, France; tassango@ijclab.in2p3.fr

\* Correspondence: cecile.gautheron@universite-paris-saclay.fr

**Abstract:** Quantifying geological processes has greatly benefited from the development and use of thermochronometric methods over the last fifty years. Among them is the (U-Th)/He dating method, which is based on the production and retention, within a crystal structure, of radiogenic <sup>4</sup>He atoms associated with the alpha decay of U, Th and Sm nuclei. While apatite has been the main target of (U-Th)/He studies focusing on exhumation and burial processes in the upper levels of the continental crust (~50–120 °C), the development of (U-Th)/He methods for typical phases of igneous and metamorphic rocks (e.g., zircon and titanite) or mafic and ultramafic rocks (e.g., magnetite) over the last two decades has opened up a myriad of geological applications at higher temperatures (>100–300 °C). Thanks to the understanding of the role of radiation damage in He diffusion and retention for U-Th-poor and rich mineral phases, the application of (U-Th)/He thermochronometry to exhumation processes and continental evolution through deep time is now mainstream. This contribution reviews the (U-Th)/He thermochronometer principle and the influence of radiation damage in modifying the diffusion behavior. It presents applications of (U-Th)/He dating to problems in tectonic and surface processes at shallow to middle crustal depths (>100–300 °C). New and promising applications using a combination of methods will stimulate a research avenue in the future.

**Keywords:** (U-Th)/He; thermochronology; zircon; titanite; magnetite; radiation damage



**Citation:** Gautheron, C.; Hueck, M.; Ternois, S.; Heller, B.; Schwartz, S.; Sarda, P.; Tassan-Got, L. Investigating the Shallow to Mid-Depth (>100–300 °C) Continental Crust Evolution with (U-Th)/He Thermochronology: A Review. *Minerals* **2022**, *12*, 563. <https://doi.org/10.3390/min12050563>

Academic Editor: Jim Lee

Received: 21 March 2022

Accepted: 27 April 2022

Published: 29 April 2022

**Publisher's Note:** MDPI stays neutral with regard to jurisdictional claims in published maps and institutional affiliations.



**Copyright:** © 2022 by the authors. Licensee MDPI, Basel, Switzerland. This article is an open access article distributed under the terms and conditions of the Creative Commons Attribution (CC BY) license (<https://creativecommons.org/licenses/by/4.0/>).

## 1. Introduction

Earth's thermal structure changes through time as a result of tectonic activity. This activity is intimately linked to the dynamics of the lithosphere at plate boundaries, causing vertical and lateral movements within the crust. This leads to mountain building as well as obduction and subduction and influences the formation and evolution of cratons. In addition, climate directly impacts the evolution of topographic relief and landscape morphology through significant weathering and erosion processes. Understanding the present-day and past evolution of the Earth's crust is a fundamental question in Earth sciences that can be tackled using different methodological approaches. Among them, thermochronology has witnessed various advances with the improvement of the understanding of numerous radioisotopic systems, such as apatite U/Pb [1], alkali feldspar and muscovite <sup>40</sup>Ar/<sup>39</sup>Ar [2], as well as (U-Th)/He (e.g., [3–6]). For more than a decade, the understanding of He production and retention in a dozen mineral phases (e.g., apatite,

zircon, titanite, rutile, perovskite, magnetite and spinel) has stimulated new research avenues on the thermal evolution of the oceanic and continental crust through geological processes in the temperature range of ca. > 50–400 °C [6,7]. Combining the (U-Th)/He method on different mineral phases with higher-temperature thermochronometers (e.g.,  $^{40}\text{Ar}/^{39}\text{Ar}$  and U/Pb) has proved to improve our understanding of the thermal evolution of the deep crust (e.g., [8,9]). In contrast, when paired with other low-temperature thermochronometers (apatite fission-track (AFT) system, closure temperature of 60–120 °C [10]; zircon fission-track (ZFT) system, closure temperature of ~180 to 250–320 °C [11]), the (U-Th)/He method allows the quantitative investigation of the thermal evolution of the Earth's subsurface (upper ten kilometers; [12,13]). The study of mountain building and erosion (e.g., [7,14,15]) and the reconstruction of deep-time thermal histories (100–2000 Myr) are the main applications (e.g., [16–21]). In addition, the development of (U-Th)/He dating of new mineral phases such as magnetite, spinel and perovskite has introduced the thermochronometric investigation of the evolution of the mafic and ultramafic oceanic and continental crust [22–26]. Finally, studies examining the (U-Th)/He system in baddeleyite [27], garnet [28] and monazite [29–31] complement the list of practicable radiogenic systems available to geochronologists working in geological and planetary science in the temperature range above 100 °C. All the advances in the (U-Th)/He dating techniques and their new applications are based on research on He diffusion processes and the role of radiation damage in He retention (e.g., [32–35]).

In this review, we mainly focus on the (U-Th)/He methods applied to zircon, titanite and magnetite, referred to as ZHe, THe and MgHe, respectively, as these have proved to allow the quantification of the thermal history (>100–300 °C) of the shallow to middle depths of the continental crust. Rutile, spinel and perovskite (U-Th)/He thermochronometric systems (RHe, SHe and PHe) are also introduced to provide an overview of available applications. The methodological principles and the role of radiation damage in the diffusion and retention of He are presented. Implications for both the thermal sensitivity of (U-Th)/He thermochronometers and the interpretation of the resulting dates are summarized. Geological examples of the use of zircon, titanite and magnetite (U-Th)/He data for constraining the thermal history of the continental crust are presented, considering orogen formation, exhumation, burial history and deep-time history. Further recommendations on the use of the (U-Th)/He method are listed, and future applications are addressed.

## 2. The (U-Th)/He Thermochronometric Method

### 2.1. He Production, Ejection and Associated Radiation Damage

Accessory mineral phases incorporate U, Th and Sm within their crystalline structure at the levels of ppb (magnetite and spinel), ppm (rutile, titanite and perovskite) and thousands of ppm (zircon). Over time, through the natural process of radioactive decay, unstable atomic nuclei of some forms of these elements ( $^{235}\text{U}$ ,  $^{238}\text{U}$ ,  $^{232}\text{Th}$  and  $^{147}\text{Sm}$  radionuclides) lose energy by emitting energetic alpha particles through the mineral medium. Each of the ejected particles is made of a  $^4\text{He}$  nucleus and travels from the location of its parent radionuclide within the medium into adjacent matter before stopping. Along its ejection path, the  $^4\text{He}$  nucleus interacts with the crystal structure and captures two electrons to become a  $^4\text{He}$  atom. Alpha particle energy, also referred to as kinetic or incident particle energy, varies as a function of decaying radionuclides and is found at the MeV level [36,37]. The kinetic energy of alpha particles emitted through the process of  $^{232}\text{Th}$  decay is slightly higher than that involved in  $^{238}\text{U}$  and  $^{235}\text{U}$  decay, which is itself much higher than that resulting from  $^{147}\text{Sm}$  decay. Traveling distances, also known as alpha stopping distances, vary as a function of the alpha particle energy and medium characteristics [38]. The latest estimations of the mean distances for mineral phases used in (U-Th)/He thermochronology range from 5 to 30  $\mu\text{m}$ , which represents a substantial portion of typical crystal sizes of commonly dated minerals (~100–400  $\mu\text{m}$ ). In consequence, an ejection factor ( $F_T$ ) correction was introduced to account for He loss by ejection. More details can be found in Farley et al. [38]. Typical  $F_T$  values for radiogenic  $^4\text{He}$  range

from 0.95 to 0.7, accounting for a He ejection correction of 5 to 30% [38,39]. The crystal geometry (i.e., size of the prism and possible pyramids) and distribution of U and Th within crystals have been extensively shown to be critical when determining the ejection factor (e.g., [5,40–42]). However, such a determination may not be necessary when the analyzed crystals are quite large in comparison with the ejection distance, or when the analysis is performed on crystal fragments, as is often the case for mineral phases such as titanite, magnetite or spinel [43]. Additional details can be found in the recent review paper of Flowers et al. [44].

The production of  $^4\text{He}$  atoms is accompanied by the production of alpha damage in the crystal lattice. The ejection of alpha particles and, to an even greater degree, recoiling of the coeval daughter nuclide lead to Frenkel pairs after atoms are pushed out of the lattice, leading to a small amorphized zone in the case of recoil damage. For high radiation doses, the number of vacancies and interstitial atoms can be so high that the lattice becomes unstable and ultimately turns into amorphized matter [45,46]. Such damage is by far much more frequently produced than the disorder caused by the motion of fragments recoiling away from one another as a result of spontaneous nuclear fission of  $^{238}\text{U}$ , which is localized over a zone of the crystal lattice called a fission track [47]. For instance, the spontaneous fission of  $^{238}\text{U}$  occurs  $2 \times 10^6$  times less frequently than alpha decay in zircon [48], and a similar factor can be accounted for in the different mineral phases presented in this study. For a given crystal, the bulk effective uranium (eU) content (most recent formula by Cooperdock et al. [49]:  $\text{eU [ppm]} = \text{U [ppm]} + 0.238 \times \text{Th [ppm]} + 0.0012 \times \text{Sm [ppm]}$ ) provides a proxy for the production rate of alpha particles [50]. This parameter allows us to sort mineral phases by range of content of radioactive isotopes, as displayed in Figure 1A, which ultimately corresponds to the dose rate. Figure 1 presents the range of typical effective uranium (eU) concentrations and estimated alpha damage dose values for the mineral phases of interest in this contribution.

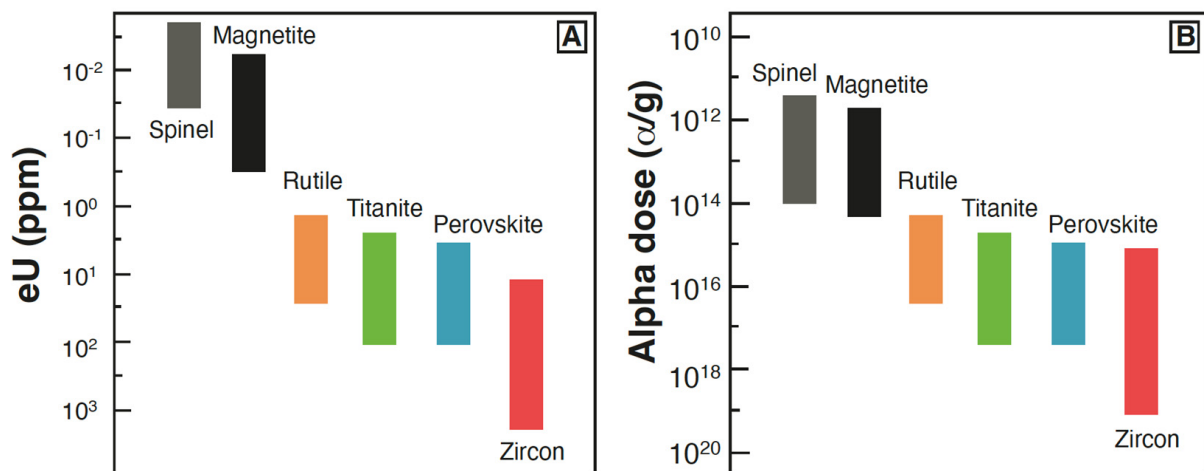


**Figure 1.** (A) Range of measured effective uranium (eU) content and (B) whole calculated alpha damage dose for an accumulation time of 1 to 2000 Myr for a variety of mineral phases of interest, for young to old thermochronometric dates. Values were computed using typical ranges obtained for those mineral phases [6,16,21,23,24,31,35,43,51].

Spinel and magnetite are very low eU mineral phases, whereas zircon shows intermediate (hundreds of ppm) to high eU contents (thousands of ppm). When integrated over the geological timescale, the accumulated alpha dose can range from low values of  $\sim 10^{10}$   $\alpha/\text{g}$  to very high values of  $\sim 10^{19}$   $\alpha/\text{g}$  (Figure 1B). Crystal metamictization, which is a gradual to complete destruction of the crystal structure associated with radiation damage, has been observed for highly damaged zircons (e.g., [52,53]) and titanites (e.g., [54,55]).

## 2.2. He Diffusion in Crystals

Within a crystal, i.e., a solid-state medium, atoms are tightly bound to each other in a regular geometric lattice characterized by structural rigidity and resistance to changes in shape or volume. Once it is produced, a He atom is incorporated into a stable vacant site between the atoms of the crystal structure, i.e., an interstitial site in the regular crystal lattice. The site is stable because, for a motion toward any direction, the atom is repelled back by the neighboring atoms of the lattice. As a consequence, the interstitial site has minimum energy. The inserted atom is shaken by the thermal motion and may gain sufficient energy to overcome the repulsion and jump to a neighboring vacant interstitial site. This is how He atoms diffuse in crystals as a random walk between sites. The hopping rate depends on the temperature and the energetical barrier between interstitial sites (referred to as the migration energy). Helium diffusion in crystals can be either isotropic or anisotropic, depending on migration energy values along the three crystallographic axes  $a$ ,  $b$  and  $c$  [51,56]. The volume diffusion rate follows the Arrhenius equation, with the migration energy being the activation energy ( $E_a$ ):

$$\frac{D}{a^2} = \frac{D_0}{a^2} \times \exp(-E_a/RT) \quad (1)$$

where  $D$  is the diffusion coefficient,  $D_0$  is the frequency factor,  $E_a$  is the activation energy,  $a$  is the diffusion domain length,  $R$  is the perfect gas constant and  $T$  is temperature. The length parameter  $a$  characterizes the diffusion domain, but the actual shape of this domain need not be specified further. Natural minerals are characterized by a habitus different from a sphere. However, it has been demonstrated that a sphere having the same surface/volume ratio as the mineral crystal is a valid approximation [42,57,58]. For anisotropic diffusion, it has been proposed to use an active radius, noted  $a'$ , which approximates anisotropic diffusion for any geometry as a simple isotropic case in a sphere [57].

In natural crystals, various studies have emphasized the role of damage (i.e., point defects, recoil damage and voids) in affecting He diffusion [5,16,33–35,59]. As stated in Section 2.1., the damage content in minerals is not null and affects the diffusion coefficient. Under the irradiation by the  $\alpha$ -particles and the daughter recoils, some atoms of the lattice can be knocked out, leaving vacancies, also named point defects. When the density of point defects is high, as in the case of those created by recoils, the lattice is locally strongly damaged and transformed into extended defects, also named radiation damage with larger voids. When a He atom falls into a defect, the energy needed to extract it is higher, compared to an interstitial site. The reason is that when moving to the neighboring site, the atom is less helped by the repulsion of back atoms because they are more distant. This is the origin of the trapping effect of defects, and the larger the defect, the stronger its trapping effect. The diffusion coefficient of a damaged crystal,  $\tilde{D}$ , can be written, following the equation of Gerin et al. [34], as

$$\frac{\tilde{D}}{a^2} = \frac{D_0 \times \exp(-E_a/RT)}{a^2 \times (1 + h \times \exp(-\Delta E_a/RT))} \quad (2)$$

where  $h$  is the damage fraction ranging from 0 to 1, and  $\Delta E_a$  is the additional trapping energy needed to diffuse out of a damage site. The damage fraction value depends on the U, Th and Sm contents, as well as the number of displaced atoms produced per decay through time [34]. It ranges from  $\sim 10^{-6}$  up to  $> 0.1$  in U-Th-rich mineral phases such as zircon [52,60], and it seems that in very low damage phases, He diffusion is significantly affected by point defects and radiation damage (see, for instance, the diffusion study of [61] in magnetite).

Figure 2A,B provide a review of the He diffusion pathway at the atomic level, between interstitial sites and damage sites. Initially, a He atom occupies an interstitial site of the crystal structure, which is characterized by an insertion energy ( $E_{ims}$ ), which is the energy needed to bring the He atom from outside or a large cavity to an interstitial site in the

crystal. This energy has to be paid to overcome the intrinsic strain in the crystal produced by the repulsion from the lattice atoms around the interstitial site [56]. The insertion energy is not null, as shown in Figure 2B, and the value is specific to each mineral. While vibrating, the He atom moves into a neighboring vacant interstitial site as a function of temperature, with a migration energy that corresponds to the activation energy  $E_a$  in the case of isotropic diffusion (Equation (1)). The migration energy is the energy necessary for a He atom to jump to the next site, which could be an interstitial site or a damage site. Figure 2A,B present the diffusion pathway of a He atom, with the energy evolution for the considered diffusion pathway. On the diffusion pathway, the He atom may encounter damage, where it is particularly stabilized. Thus, an additional energy ( $\Delta E_a$ ; Equation (2)) will be necessary to move the He atom back into a neighboring vacant interstitial site [33]. This is the consequence of the lower insertion energy of the damage site compared to that of the interstitial site [34,51].

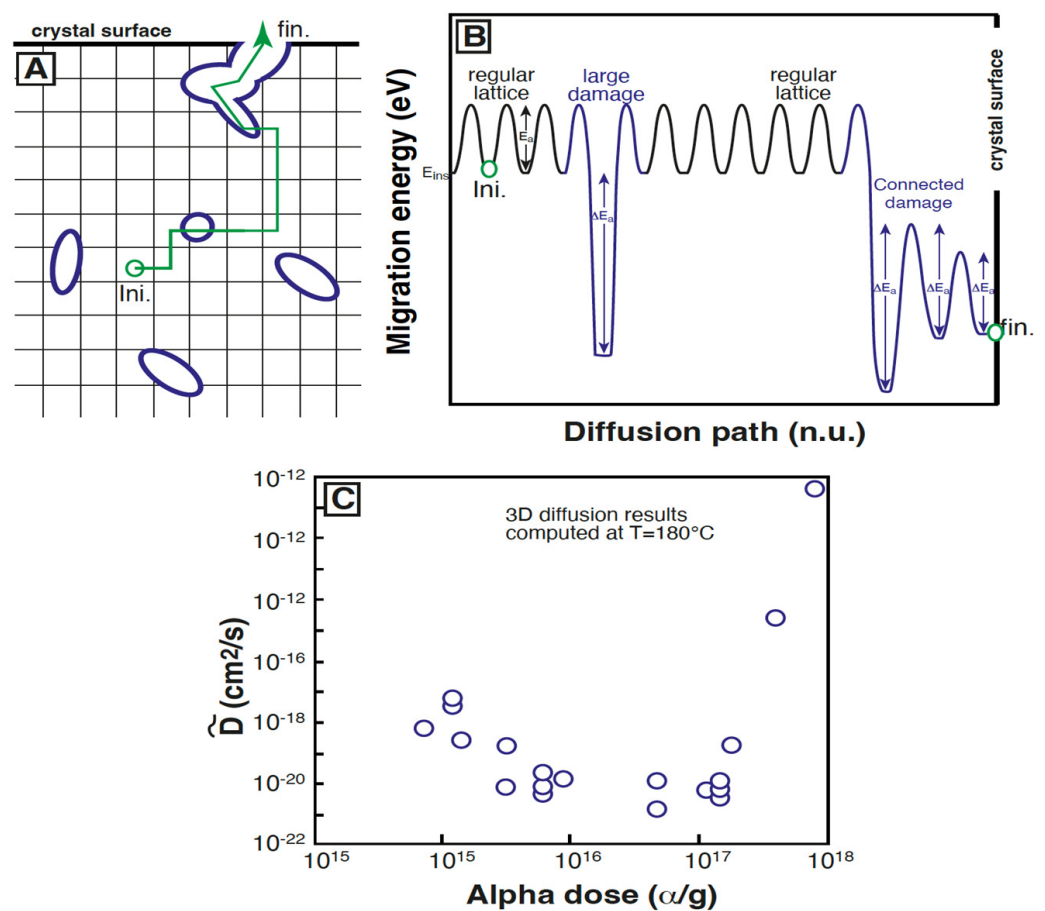


**Figure 2.** (A) Schematic representation of a diffusion pathway for He (green ball) and (B) resulting He energy evolution for this considered diffusion pathway. The energetic levels are the insertion energy,  $E_{ins}$ , the migration energy between interstitial sites,  $E_a$ , and the trapping energy that is needed for a He atom trapped in a damage site to jump back to an interstitial site,  $\Delta E_a$ . In a damage zone, the He insertion energy is lower, and the resulting trapping energy will increase. Adapted from [51]. (C) He diffusion coefficient ( $\tilde{D}$ ) for damaged zircon as a function of the alpha damage dose; from [35] and references therein.

Eventually, the He atom reaches the crystal surface and can come out of the crystal. As shown in Figure 2C, which reports the diffusion coefficients ( $\tilde{D}$ ) computed at 180 °C for different zircon crystals, bulk 3D diffusion is a function of the damage dose. For alpha doses lower than  $\sim 10^{16}$   $\alpha/g$ ,  $\tilde{D}$  decreases with increasing damage dose as a result of the trapping effect of radiation damage. Once a damage dose threshold is reached ( $\sim 10^{16}$   $\alpha/g$ ),

the diffusion coefficient increases due to damage percolation, as the latter forms some type of fast diffusion path [35,62]. The diffusion coefficient evolution thus results from the combination of both the trapping energy and the damage dose in mineral phases.

### 2.3. Thermal Sensitivity of He in Crystals and Impact on (U-Th)/He Ages

Helium retention in crystals depends on the nature of the mineral phase, crystal size, thermal history and crystal-dependent diffusion coefficient,  $\tilde{D}$  (this coefficient is intimately linked to the previous three dependencies plus damage, itself depending on the thermal history through damage annealing; see Equation (2)). For two crystals of the same size which share a similar thermal history, He retention (as well as accumulation and diffusion) can therefore significantly differ from one case to another. To illustrate such a variable He thermal sensitivity, it has been common to use the closure temperature,  $T_c$ , which is an empirical value introduced by [63] to conveniently describe the temperature retention range for a specific thermochronometer.  $T_c$  is defined as the temperature corresponding to the apparent (U-Th)/He age for a temperature decreasing linearly. For such a monotonic cooling, it characterizes the temperature at which 50% of the produced He atoms are retained in the crystal (Figure 3A). A closure temperature is rarely equivalent to the age at which a crystal crosses the associated isotherm during cooling, as explained in [64]. Associated with the concept of the closure temperature, the helium partial retention zone (He-PRZ) represents the temperature window in which 10 to 90 % of the produced He atoms are retained in the crystal during cooling [65]. For temperatures above the He-PRZ, the produced He atoms are not retained in the crystal during geological time (Figure 3A). In strict terms, the diffusion of He atoms out of the crystal structure outpaces the accumulation of He atoms within the crystal lattice.

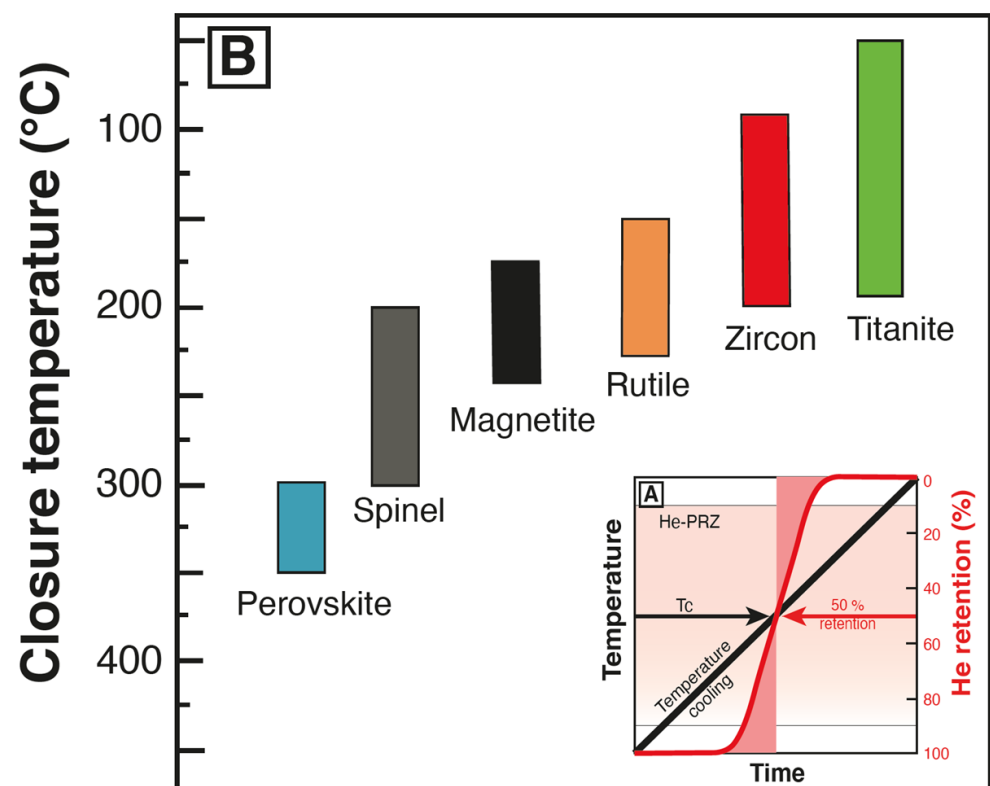


**Figure 3.** (A) Schematic evolution of the He content retained for a monotonic cooling, with the definition of the closure temperature and the He-PRZ (partial retention zone). (B) Closure temperature range for selected minerals. Note the reversed scales, suggesting relative depths.

In the early days of (U-Th)/He thermochronology, a unique He diffusion coefficient was retrieved, often from volcanic standard minerals (e.g., [4,22,66,67]). However, with the ever-increasing volume of diffusion data and variety of geological applications, the role of damage in altering He diffusion has been highlighted for different mineral phases such as zircon [18,35,51], titanite [16,18], rutile [21] and magnetite [61]. Equivalent investigations are still required for perovskite [26] and spinel, for which  $T_c$  is based on empirical constraints comparing spinel (U-Th)/He and zircon fission track results [23].

Closure temperature ranges are reported for six selected mineral phases in Figure 3B, considering typical crystal sizes.

In zircon,  $T_c$  increases from ~100 °C to 200 °C for low ( $<10^{15}$   $\alpha/g$ ) to intermediate radiation damage ( $<10^{17}$   $\alpha/g$ ) [35,68,69] and decreases down to  $<100$  °C for damage doses above a radiation damage threshold value estimated at  $2 \times 10^{17}$   $\alpha/g$  [51,62]. The strong influence of damage on He diffusion in zircon leads to very dispersed ZHe apparent ages, which carry information on the thermal history (e.g., [8]). Similarly, the titanite  $T_c$  evolves with the damage dose from 190 to 200 °C at low doses [70] down to very low temperatures at high doses ( $<50$  °C; [16]). Inverse age–eU correlations with highly dispersed ages are commonly found in titanite, resulting from variations in radiation damage [16,18,71]. Rutile displays a  $T_c$  ranging from ~150 to 200–230 °C [70], and a recent study emphasized a possible increase in the rutile  $T_c$  with increasing radiation damage [21]. In magnetite, a  $T_c$  of 250 °C has been suggested [22], but the influence of radiation damage has been proposed to expand the  $T_c$  range from 150 up to  $<275$  °C [61]. In spinel and perovskite,  $T_c$  is constrained empirically using geological data, with estimations given at 200–300 °C and  $>300$  °C, respectively [23,26].

#### 2.4. Reviewing the Origin of (U-Th)/He Date Variation

A (U-Th)/He apparent age (i.e., date) is a net balance between He production and accumulation efficiency within a crystal for which the raw date is corrected for alpha ejection using the ejection factor ( $F_T$ ). A discussion about the most appropriate way to correct a (U-Th)/He date can be found in Flowers et al. [44]. Helium accumulation within a crystal depends on the diffusion coefficient value, itself a function of the thermal history and size of the crystal. An illustration of the effect of damage on the diffusion coefficient, and consequently He-PRZ boundaries,  $T_c$  and (U-Th)/He ages, is presented in Figure 4. For two theoretical thermal histories, the evolution of the diffusion coefficient for low- and high-eU crystals of a given mineral phase, as well as relative changes in (U-Th)/He dates with increasing radiation damage dose, is displayed. The first thermal scenario consists of a monotonic cooling, while the second includes a long exposure to temperatures within the He-PRZ.

In the first thermal scenario (Figure 4A), low- and high-eU crystals are at a temperature above the He-PRZ before cooling. During the stage at high temperature, the produced He atoms diffuse out of the crystals and the associated radiation damage anneals. Low- and high-eU crystals have the same constant diffusion coefficient value. During the cooling phase, annealing diminishes, radiation damage starts to accumulate in the crystals and  $\tilde{D}$  decreases linearly with decreasing temperature for the two types of crystals. As a consequence of damage accumulation,  $\tilde{D}$  depends on the damage dose. In particular, the higher the bulk eU content of the crystals, the lower the diffusion coefficient. Nevertheless, the difference in diffusion coefficient values for low- and high-eU crystals remains small. Despite their dependency on the crystal size and eU content, (U-Th)/He dates turn out to be overall little dispersed, albeit younger at a low eU content. This example is valid for any mineral phase, though date dispersion in perovskite, magnetite and spinel (low-eU mineral phases) is expected to be lower than that in zircon, titanite and rutile (higher-eU mineral phases).



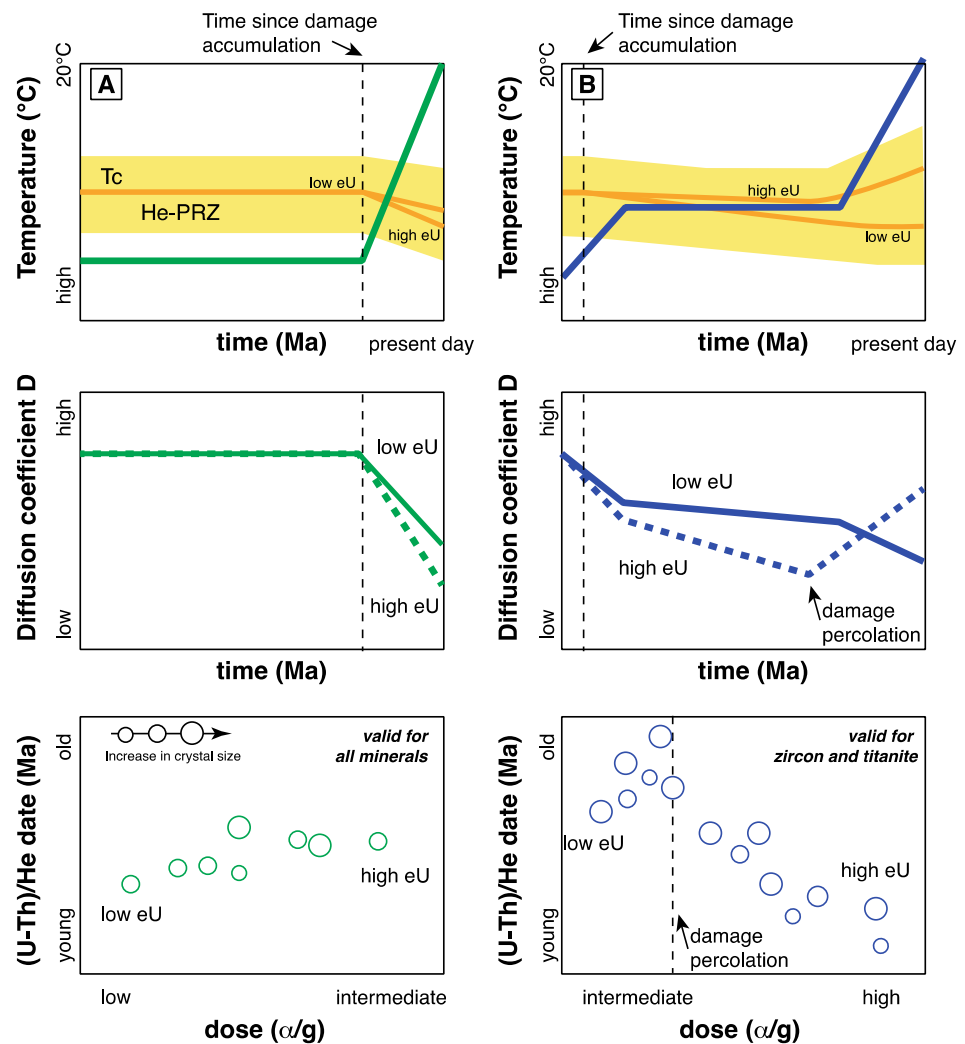


**Figure 4.** Schematic evolution of the He-PRZ (partial retention zone), closure temperature ( $T_c$ ), diffusion coefficient ( $\bar{D}$ ) and (U-Th)/He date for different crystal sizes (equivalent spherical radius  $R_s = a$ ) for two end-member thermal histories: (A) monotonic cooling, and (B) long stay in the He-PRZ.

In the second thermal scenario (Figure 4B), two distinct phases of cooling are separated by a long exposure to temperature conditions within the He-PRZ. The first cooling phase causes low- and high-eU crystals to enter the He-PRZ, which results in decelerating rates of both diffusion of He atoms out of the crystals and annealing of radiation damage. During this phase, the diffusion coefficient decreases with decreasing temperature for the two types of crystals, albeit in a slightly steeper manner for higher-eU crystals. This is fairly similar to what is depicted for the period of cooling in the first thermal scenario. During the subsequent long residence time at a constant temperature in the He-PRZ, the diffusion coefficient continues to decrease for the two types of crystals, in a manner that is consistent with the continued accumulation of damage in crystals. This decrease is much steeper than the previous one for high-eU crystals, because of the higher amounts of damage produced in higher-eU crystals. During the second phase of cooling, the diffusion coefficient continues decreasing for low-eU crystals, but it increases for high-eU crystals. As a result of the higher amount of the accumulated damage dose and lower diffusion coefficient values compared to case A (Figure 4A), the He-PRZ and  $T_c$  drop with time. In U-Th-rich mineral phases such as zircon, titanite and, to a lesser extent, rutile, the damage dose is intermediate to high. In these high-eU mineral phases, a plot of (U-Th)/He dates against the damage dose presents a positive correlation at intermediate doses, and

a negative correlation at intermediate to high doses (Figure 4B). These correlations peak at a dose that corresponds to the damage percolation threshold. As the bulk effective uranium content provides a proxy for both the alpha particle production rate and the relative amount of accumulated, non-annealed damage, positive and negative date–eU correlations are also expected, resulting in significant dispersion of (U-Th)/He dates in a sample. Overall, the simulation for high-eU crystals shows that the longer the exposure of the crystals to temperatures within the He-PRZ, the higher the accumulation of damage within these crystals, and consequently the higher the dispersion of their (U-Th)/He dates. In contrast, for lower-eU mineral phases such as spinel, magnetite and perovskite, the radiation damage dose is always low to intermediate. Therefore, only a positive date–dose, or date–eU, correlation is expected, with relatively low date dispersion.

Examples of geological applications of the concepts discussed above presented in Sections 3 and 4 more quantitatively present the evolution of (U-Th)/He dates, and how date dispersion is used to better refine the thermal history investigation.

### 2.5. Analytical Subtleties

Crystals are manually extracted from rocks and isolated using conventional mineral separation methods. These include crushing, grinding, sieving, water table concentration, standard heavy-liquid density and magnetic susceptibility separation techniques [5]. Crystals are subsequently handpicked according to strict criteria for (U-Th)/He analysis [44]. Selected crystals can be further analyzed for mineralogical and geochemical purposes using Raman spectroscopy, SEM backscattered electron imaging, electron microprobes and laser ablation inductively coupled plasma mass spectrometry (LA-ICP-MS) [25,72]. For idiomorphic crystals, dimensions of the prism (length, width and thickness) and pyramids are determined by direct optical measurement or picture-based volume reconstruction [73], micro-X-ray tomography [74] and CT scan (computed tomography, [49]) techniques. The crystal size and geometry are used to determine the ejection factor ( $F_T$ ), the equivalent spherical radius ( $R_s$  or ESR) and the weight of crystals in micrograms (i.e., zircon, rutile, titanite and perovskite). For some crystals, the weight can also be determined with higher precision using the isotopic dilution method [75].

Single crystals (aliquots) are packed into a niobium (Nb) or platinum (Pt) tube, whereas larger crystals or multi-aliquots are wrapped into Nb foils. They are then placed under vacuum for degassing and He content analysis using quadrupole or magnetic sector mass spectrometers (e.g., [76,77]). Special care for possible U and Th volatilization during crystal heating should be taken into account for some mineral phases such as rutile (e.g., [21]). For U-Th-rich phases such as zircon and titanite, in situ He analysis using LA-ICP-MS is also possible [78]. Once analysis is complete, the Nb/Pt capsules or Nb foils are retrieved from the ultrahigh vacuum chamber for wet chemistry digestion and determination of U, Th and Sm (if possible) concentrations using inductively coupled plasma mass spectrometry [79]. U-Th and Sm contents can also be determined in situ using LA-ICP-MS analysis [78], allowing additional analyses of, for example, U-Pb and Hf isotopic compositions or rare-earth element abundances to be performed on the same crystals (e.g., [80,81]). As Sm is a minor contributor to the alpha particle (alternatively He) production budget, its content is not often determined for U-Th-rich mineral phases. Replicate analysis of standard mineral materials is performed during the analytical batch to ensure the data quality and to estimate analytical uncertainties. Standards include Fish Canyon Tuff zircon, and zircon and titanite from Limberg samples [82–84]. When analyzing rutile, perovskite, magnetite and spinel for (U-Th)/He, an in-house mineral material that has been previously documented in geological studies is used to track technical and methodological problems (e.g., [22,26]).

Once measured, He, U, Th and Sm contents (e.g., mol, ng) are used to calculate a raw, uncorrected (U-Th)/He date [85], and the He, U, Th and Sm of a crystal are converted into concentrations (e.g., mol/g, ppm) using the weight of the crystal. The typical analytical  $1\sigma$  standard error for raw dates ranges from ~5 to 10%, which is generally lower than natural

age dispersion [6,30]. (U-Th)/He dates are finally corrected for alpha loss using the  $F_T$  value [38] when necessary (see Section 2.1).

### 2.5.1. eU-Rich Mineral Phases

For U-Th-rich mineral phases such as zircon and titanite, alpha implantation from neighboring phases is negligible, and the main sources of (U-Th)/He date variation are the crystal size, parent nuclide zoning and radiation damage (see Sections 2.1–2.4; [5]). U-Th zoning can be quite important, especially in zircon, and an adequate ejection factor should be applied [41]. However, it must be acknowledged that in conventional bulk ZHe dating studies, the degree of zonation within each of the dated crystals is rarely measured due to intrinsic analytical protocol limitations. Titanite can be rich in inclusions that contain considerable amounts of U and Th and are not digested in the acid mix used for chemical dissolution of titanite (notably zircon and rutile). Inclusion-free titanite fragments should therefore be selected for THe dating. Furthermore, these fragments should be devoid of outer crystal surfaces, as erroneously young ages could be obtained otherwise [4,43]. Moreover, as is typical in titanite, U and Th, heterogeneities can cause variation in the He content, resulting in excessive date dispersion. LA-ICP-MS should therefore be used to investigate the overall parent nuclide homogeneity of the crystals.

Finally, the amount of damage in U-Th-rich mineral phases is often high ( $>10^{17}$  to  $10^{19}$   $\alpha/g$ ; Figure 1). The crystal color has been reported as a first-order indicator of the radiation damage density in zircon [86]. Raman spectroscopy can also be used to determine radiation damage in zircon [52,53,87] and titanite [54,55,71,88,89] as these mineral phases show important Raman band broadening with increasing damage density (Figure 5A). Thus, correlation of THe ages with the calculated damage dose or Raman band broadening could be performed, as illustrated in Figure 5B,C.

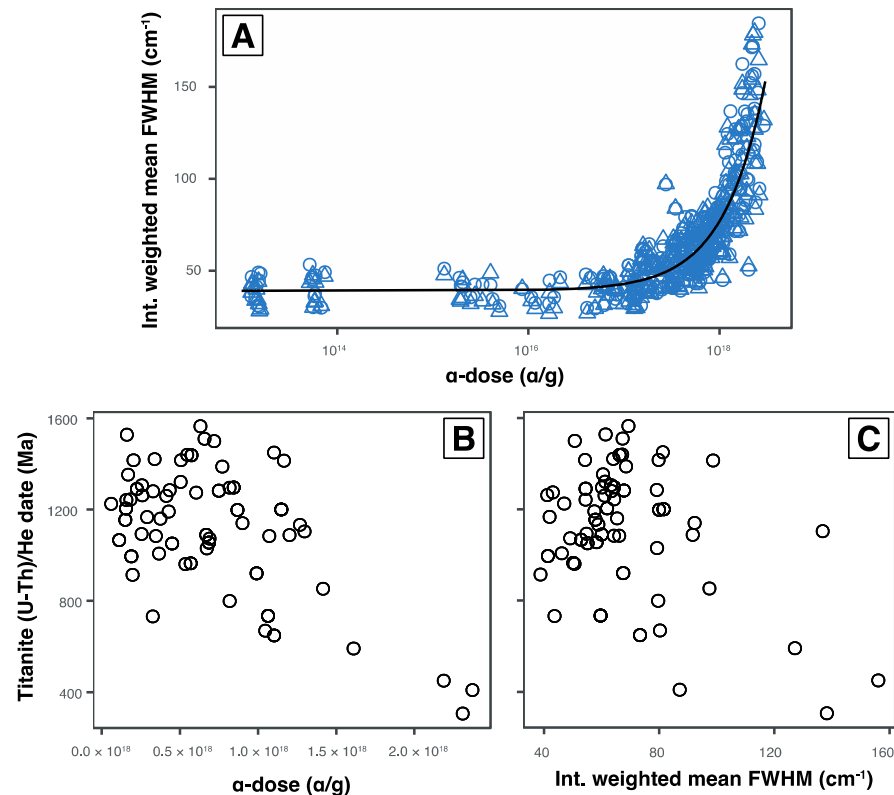


**Figure 5.** (A) Calibration of  $\alpha$ -dose and Raman bandwidth (expressed as intensity-weighted mean FWHM (full width at half maximum)) for titanite as proposed by Heller et al. [71]. (B) Relation of titanite (U-Th)/He dates and  $\alpha$ -dose, and (C) mean Raman bandwidth for the same dataset. Adapted from [71].

Because Raman spectroscopy is a time-efficient, cheap and non-destructive method, for which there are empirical calibrations available for both zircon [52,53,90] and titanite [71], it represents a valuable tool for damage-based selection of crystals for thermochronology. Depending on the target of a study, poorly or highly damaged crystals can be chosen using this tool. In the case of zircon, there is furthermore the possibility of calculating zircon damage dates [91–93], which can be an interesting complement to ZHe dating [94]. According to Hartel et al. [92], the zircon damage  $T_c$  ranges from 260 to 370 °C and is therefore slightly higher than the ZHe  $T_c$ .

### 2.5.2. eU-Poor Mineral Phases

In addition to the crystal size, parent nuclide zoning and radiation damage, alpha implantation from U-Th-richer mineral inclusions or neighboring mineral phases may represent a significant source of date variability for U-Th-poor mineral phases. This can affect the He content of the dated crystals significantly, as firstly demonstrated for apatite (e.g., [95]). For transparent mineral phases such as rutile, careful selection of the crystals can limit the effect of mineral inclusions, but implantation should be investigated petrologically. For opaque mineral phases such as magnetite and spinel, only CT scan analysis can reveal mineral inclusions inside the selected crystals [24,49]. Petrological analysis of rocks containing the dated crystals could additionally bring important information and reveal their crystallization environment.

As an example, Schwartz et al. [25] performed magnetite (U-Th)/He (MgHe) dating of euhedral and pseudo-euhedral crystals (Figure 6A) from an exhumed high-pressure ophiolite from the Western Alps (France). Euhedral MgHe dates ranged between the ZFT and AFT ages, which is in agreement with the known closure temperature of the MgHe system [25]. In contrast, pseudo-euhedral crystals yielded MgHe dates that are older than ZFT (Figure 6A), suggesting the impact of alpha implantation from eU-rich neighboring crystal phases (Figure 6B).

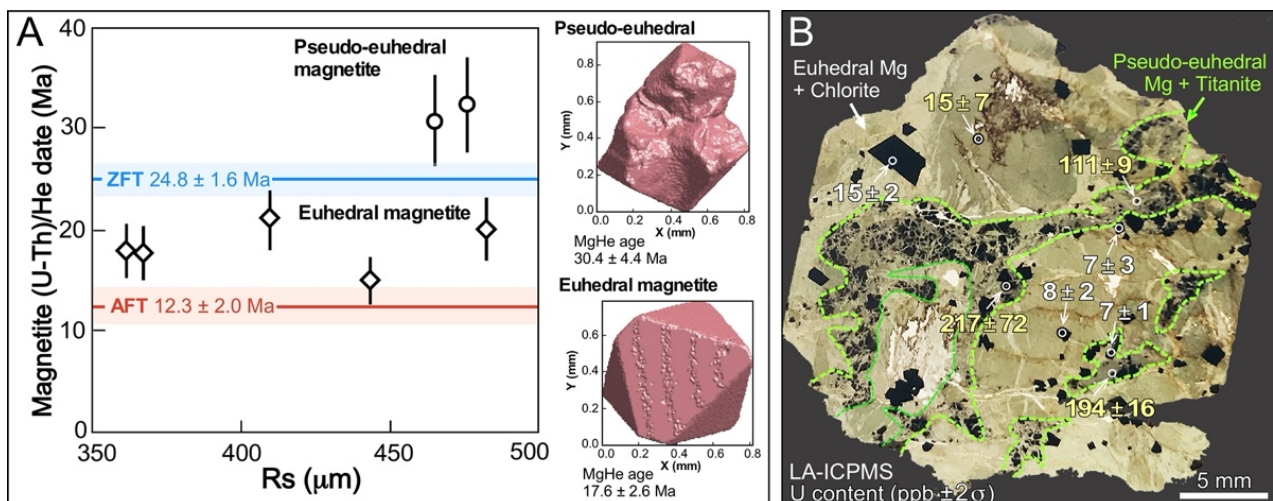


**Figure 6.** Magnetite (U-Th)/He results for HP ophiolite from the Western Alps. (A) MgHe dates obtained on euhedral and pseudo-euhedral crystals with 3D reconstructions from computed tomography scan images of each euhedral and pseudo-euhedral crystal plotted versus the crystal sphere equivalent radius ( $R_s$ ), together with apatite fission track (AFT: pink band) and zircon fission track (ZFT: blue band) date ranges from [96]. (B) In situ measured U concentration of magnetite, chlorite and titanite from titanite-rich zones and chlorite-rich zones in which pseudo-euhedral and euhedral magnetite crystals are identified, respectively. U content obtained from neighboring minerals (chlorite or titanite) are reported in yellow. Adapted from [25].

Petrological investigation of the sample and in situ measurement of the U content revealed that euhedral magnetite crystallized in association with chlorite, whereas pseudo-euhedral magnetite crystallized in zones surrounded by titanite (Figure 6B). In addition, whereas euhedral magnetite and chlorite have similar U contents, the U content in titanite is significantly higher than in the associated pseudo-euhedral magnetite (Figure 6B). Taken together, these observations suggest that alpha implantation from neighboring titanite into pseudo-euhedral magnetite was significant, thus resulting in much older MgHe dates for pseudo-euhedral crystals (Figure 6A). This study reveals that mineralogical environment characterization is of uttermost importance to interpret (U-Th)/He data from eU-poor mineral phases, especially in metamorphic rocks.

### 2.6. Subtleties of Thermochronological Ages and Interpretation

(U-Th)/He data carry information on the thermal history of a sample and should be interpreted in light of current thermochronological models, especially that of He diffusion behavior in the analyzed mineral phases. Investigation of the dependencies of (U-Th)/He dates with the eU concentration, crystal diffusional volume ( $R_s$ ) and Th/U ratio should be performed first and routinely. Alpha dose calculation is an option that allows the observation of possible date evolution for different samples, providing that the time period for damage accumulation is known. These pieces of information are useful to identify date evolution patterns (e.g., date–dose or date–eU correlations) that help model the thermal history of the sample.

Thereafter, date investigation should be continued through thermal history modeling of data using 2D modeling software such as HeFTy [97] and QTQt [98], or a 3D thermo-kinematic approach (PECUBE [99]). A radiation damage He diffusion algorithm should be used when available; otherwise, the He diffusion coefficient should be adapted. For zircon, the RDAAM algorithm implemented in HeFTy and QTQt successfully reproduces most of the ZHe data [35,69], except for highly damaged crystals (e.g., [94]). Additional work shows that He diffusion could be slightly more complex [51,68]. New damage annealing studies [100] will certainly stimulate the development of a better damage production and annealing model for zircon. A first attempt to model He diffusion in magnetite has been performed [61] from diffusion data [22]. However, no damage model exists for titanite and rutile, limiting the quantitative modeling of (U-Th)/He data for these phases.

## 3. Recovering Thermal History through (U-Th)/He Data Inversion

### 3.1. On the Record of the Different Stages of Orogenesis in the Pyrenees by ZHe Dating and Subordinate Thermochronometric Systems

Together with the ever-increasing analytical capabilities, the investigation of orogenic processes has led to flourishing advances in the conceptual, methodological and technical development of thermochronometric systems, especially ZHe. This has, in turn, stimulated new research avenues, for instance, on crustal thermal and dynamic behavior during orogenesis in low-extension, low-convergence orogens. Here, we review an example of the application of (U-Th)/He thermochronometry in the Pyrenees, southwestern France. In the easternmost part of the mountain range, bedrock ZHe dating has recently proved to allow the detection of middle–lower crust exhumation during rifting/hyperextension (when combined with apatite U/Pb analysis; [8,101]) and subsequent early crustal growth of a collisional orogen (when combined with AHe and AFT dating; [8]).

Ternois et al. [8] provided a detailed bedrock, single-grain ZHe and AHe dataset from a crustal block from the Agly-Salvezines Massif (eastern Pyrenees, France) that is believed to have occupied the distal end of the European rifted margin. AHe dates of this dataset fall into the range of previously published bedrock AFT dates for the block [102,103], indicating fairly rapid cooling below temperatures of 110–45 °C during the early-middle Eocene. In contrast, the ZHe dataset shows a high degree of date variability (~57 to 117 Ma), with significant intrasample variation (~19 to ~93%), as presented in Figure 7. All ZHe dates are older than AHe [101] and AFT dates [102,103], and the oldest ZHe dates overlap with

bedrock apatite U/Pb dates [101]. As highlighted by Ternois et al. [8], ZHe dates thus span within error the time interval between the onset of rifting and associated thermal events ( $\sim 117$ – $114$  Ma, e.g., [104–107] and references therein), and the onset of the main collision in the Pyrenean region ( $\sim 50$  Ma, e.g., [108,109] and references therein).

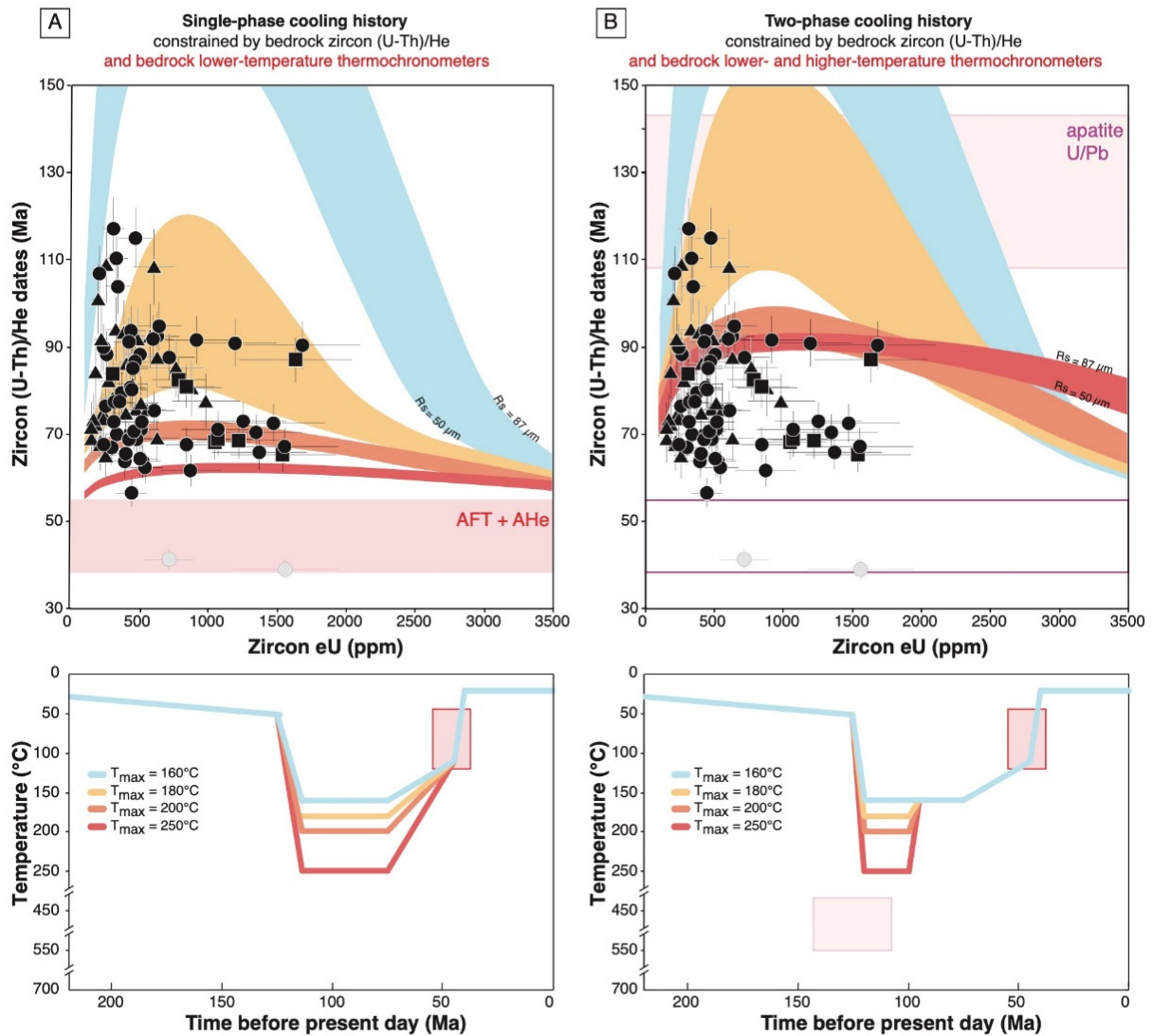


**Figure 7.** Comparison of the bedrock zircon (U-Th)/He age–eU correlations for the dataset obtained from the Agly-Salvezines Massif (eastern Pyrenees, France) crustal block with forward models simulating either (A) a single-phase cooling history constrained at low temperatures by apatite fission track and (U-Th)/He data, or (B) a two-phase cooling history constrained at high temperatures by apatite U/Pb data, and at low temperatures by apatite fission-track and (U-Th)/He data. The bottom two panels show five different t–T scenarios with either (A) Late Cretaceous cooling at 75 Ma or (B) middle Cretaceous cooling from 100 to 95 Ma followed by Late Cretaceous cooling at 75 Ma. The resulting zircon (U-Th)/He age–eU envelopes [8] are plotted in the two top graphs with the color of each envelope matching a specific t–T path. Envelopes encompass the 2-standard-deviation grain sizes ( $69 \pm 18 \mu\text{m}$ ) observed by Ternois et al. [8], so that the upper and lower bounds of the color envelopes correspond to the age–eU curve that would be produced for a grain size of 87 and 50  $\mu\text{m}$ , respectively. Pink boxes in the top and bottom panels indicate radiometric age ranges and associated closure temperature windows for major thermal and tectonic events from the literature [8,101]. Adapted from [8].

Overall, bedrock ZHe results display first-order positive and negative date–eU correlations, with dates of ~90–120 Ma around the maximum of these correlations (eU content of 250–600 ppm) and exceptionally consistent dates of ~65–75 Ma around their respective minimum (Figure 7). Such a non-random distribution of ZHe dates concurs with the zircon radiation damage and annealing modeling predictions of [35], leading Ternois et al. [8] to argue for rapid crossing of the < 140–160 °C temperature window by very low and high eU zircon crystals from 75 to 65 Ma. This is consistent with an earlier start of the (U-Th)/He clock in zircon in comparison to less He-retentive apatite on a cooling path of the bedrock samples during convergence and early inversion of distal rifted margins in the Late Cretaceous (Figure 7A). Ternois et al. [8] additionally attributed a closure temperature window of 200–250 °C to the older, intermediate-eU zircon crystals, as these are predicted to be more helium-retentive and have a higher temperature sensitivity ([35]). However, the authors recognized the complexity of the pre-orogenic thermal history in the Pyrenees, as indicated by sometimes conflicting field, geochemical and radiometric data. To investigate the significance of ZHe dates, Ternois et al. [8] thus explored plausible time–temperature trajectories consistent with the data through modeling (Figure 7A,B). Combining new field and available geological and geochemical data from the literature with inverse and forward modeling of (U-Th)/He and FT data, the authors built a robust demonstration of the thermochronological record of a marked cooling event starting around the end of the Late Cretaceous as a result of early Pyrenean orogenesis.

In addition, the authors propose that an earlier, middle Cretaceous cooling history of the crustal block, possibly related to rifting and/or post-rift, is detected. Recent bedrock apatite and rutile U-Pb data ([8,101]; overall closure temperature window of ~425–550 °C, see [1] review) overlap with older ZHe dates [8] (Figure 7B), suggesting that lower- to mid-crustal levels of the block cooled rapidly to <<450 °C at the onset of rifting, after which they were never reheated to temperatures > 300 °C during Pyrenean orogenesis. Ultimately, combining forward modeling of ZHe data with apatite U/Pb data demonstrates that only rift-related exhumation can explain the cooling of the block during the middle Cretaceous, as shown in Figure 7B.

This example therefore not only shows the power of zircon (U-Th)/He dating in distinguishing the thermal signature of early orogenesis from preceding rift and subsequent thermal events in the Pyrenees but also demonstrates that bedrock zircon (U-Th)/He dates plotting at opposite ends of the eU content spectrum can be used with confidence as robust age constraints in geological reconstructions.

### 3.2. HP Ophiolite Thermal History Retrieved from MgHe Data Thermal Inversion

As shown in Section 3.1., mountain range evolution can be quantified using thermochronometers of different thermal sensitivities. However, most of the thermochronometric applications are possible thanks to the presence of apatite-, zircon- and titanite-rich rocks such as felsic rocks. With the development of magnetite, spinel and perovskite (U-Th)/He methods, the world of mafic and ultramafic rock exhumation history is opened [23–26].

Schwartz et al. [25] presented a case study that revealed the thermal history of rocks through the use of MgHe dating from the high-pressure/low-temperature (HP-LT) Rocher Blanc ophiolite, embedded in deformed sedimentary units of the Schistes Lustrés (Western Alps, France). The study site was selected because the pressure–temperature evolutions of the Schistes Lustrés units are well documented. The early prograde phase reaches metamorphic peak conditions at 10 kbar and >350 °C [110,111], dated from 62 to 55 Ma [112]. The retrograde metamorphism stage, which remained in the field typical of greenschist paragenesis, is also known (Figure 8A). The final exhumation was constrained by apatite and zircon fission track analysis [96] (Figure 8A), which revealed a diachronous exhumation of the HP-LT metamorphic rocks from east to west during the Oligocene to Miocene. Using published cooling rates, the Rocher Blanc ophiolite is considered to have crossed the ~240–280 °C isotherm at ~25 Ma and the ~110 °C isotherm at ~12 Ma (Figure 8A).

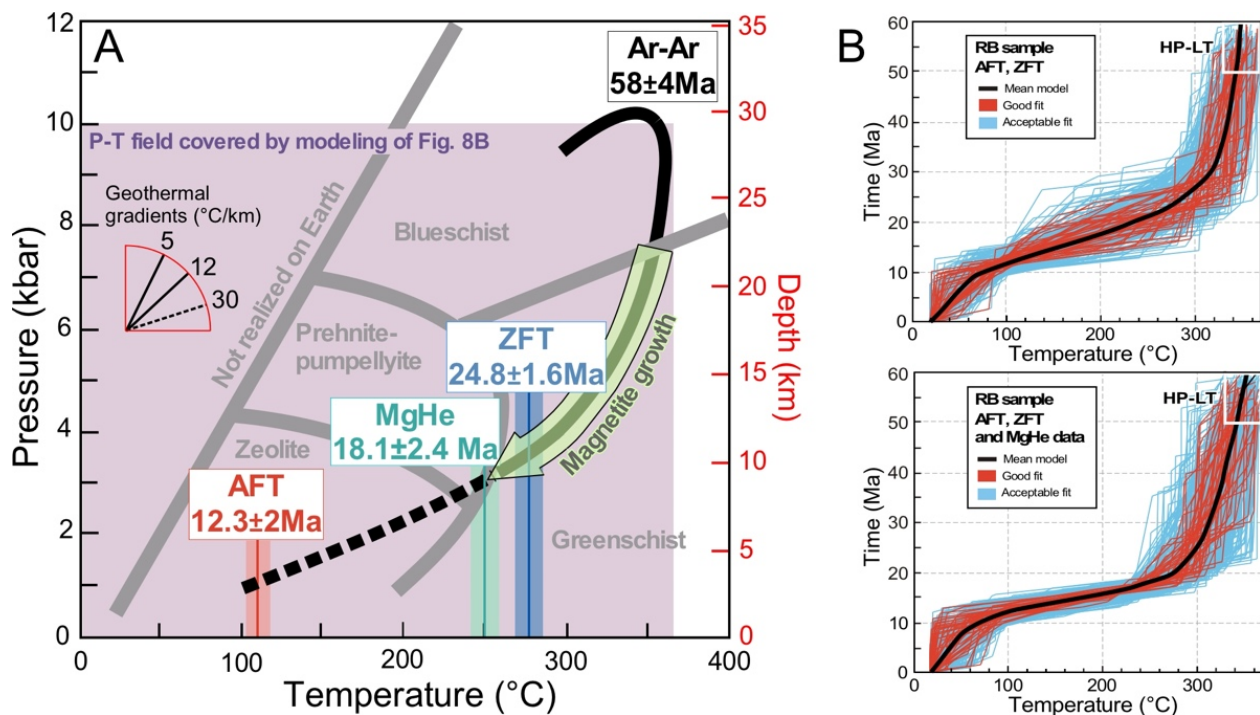


**Figure 8.** (A) Pressure–temperature path of the high-pressure/low-temperature (HP-LT) Rocher Blanc ophiolite (RB, Western Alps), in which the apatite fission track (AFT), magnetite (U-Th)/He and zircon fission track (ZFT) estimated dates are reported using their associated closure temperature conditions (see [25] for references). (B) Thermochronological data inversion modeling of the HP-LT Rocher Blanc ophiolite using the AFT and ZFT data only or AFT, ZFT and MgHe data. Note that the axes are inverted from the typical T-t diagram. Adapted from [25].

Petrological investigation of the Rocher Blanc ophiolite revealed that magnetite crystallized during retrograde metamorphism (Figure 8A). The obtained MgHe ages on euhedral magnetite crystals range from 14 to 20 Ma (Figure 6), within the range of ZFT and AFT ages, which is in agreement with the known closure temperature of the different thermochronometers [25]. These results demonstrate that magnetite recorded the cooling history during retrograde metamorphism.

Inversion of the MgHe data, along with the AFT and ZFT data, allowed the authors to better constrain the time–temperature paths of the cooling trajectory, as shown in Figure 8B. The MgHe data suggest that fast cooling had been delayed until ~20 Ma, which is later than what would be inferred from the ZFT and AFT ages alone (~26 Ma; Figure 8B). Inverse modeling of MgHe data therefore allows the quantification of exhumation processes in ductile conditions of mafic and ultramafic rocks.

### 3.3. Revealing the Deep-Time Thermal History of the Brazilian Margin through ZHe Data Investigation

Reconstruction of the thermal histories of the continental crust on the scale of hundreds of millions to billions of years, known as deep-time thermochronometry, has emerged with the ability to model He diffusion in crystals that have accumulated radiation damage (e.g., [19,33,35]). This allows geologists to decipher geological processes through geologic time [20,113], and to understand cratonic evolution and supercontinent cycles [18,114,115], or passive margin evolution [116,117]. Typically, zircon, titanite and rutile (U-Th)/He data are coupled with apatite (U-Th)/He thermochronology, which reveals the last part of the thermal history [14,114].

Hueck et al. [94] illustrated how the accumulation of radiation damage in zircon crystals can be used as a tool for reconstructing long-term thermal histories in ancient and geologically stable regions. Their study was based on a detailed ZHe and AHe



dataset from South Brazil, in an area located at the southern limit of one of the classical examples of elevated passive margins (Figure 9A,B). Because of this marginal position, the thermochronological data in this area have characteristics that are typical for both the elevated and the low-relief sectors of the South American passive margin [118]. On the one hand, the AHe data yield relatively uniform results, indicating a well-constrained post-rift exhumation of the region between the Upper Cretaceous and the Paleogene, similar to what is observed in much of the coast-parallel ridges to the north of the study area [119–122]. On the other hand, the ZHe dates are exceptionally widespread (472 to 26 Ma), showing evidence of a much older pre-rift exhumation history, which is typically recorded only in the low-elevation portions of the passive margin further to the south [118,123–126].

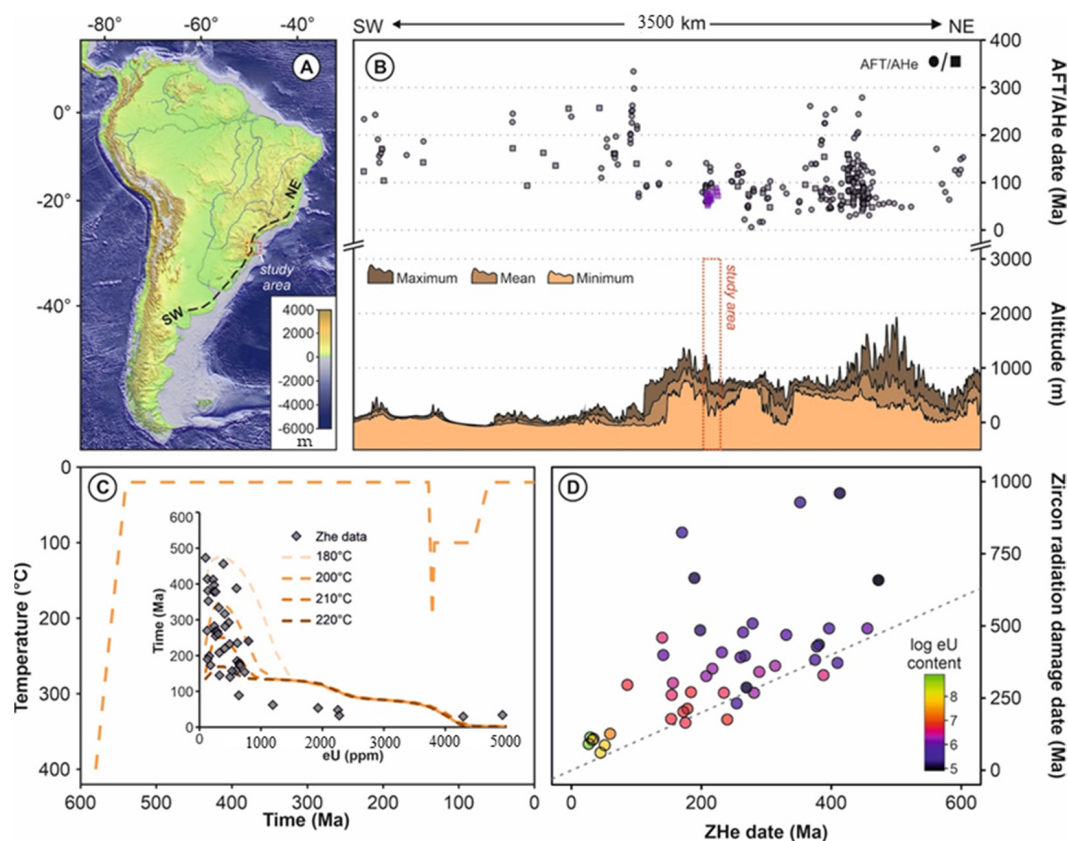


**Figure 9.** (A) Digital elevation model of South America and part of the South Atlantic Ocean with the approximate location of the cross-section in B and of the area studied by Hueck et al. [94], for which the results are synthesized in (C,D). (B) Topographic cross-section and compilation of apatite thermochronological data (apatite fission tracks (AFT) and (U-Th)/He (AHe)) along the cross-section shown in A (modified from [118]). Maximum, mean and minimum altitudes along the profile were calculated considering a 25 km buffer on both sides of the main profile line, and thermochronological data were compiled from a 50 km buffer (see [118] for source of the data). Apatite (U-Th)/He dates from the study area in C and D are not located within the area for which data are compiled in B but are represented in purple for context. (C) Forward modeling of the correlation between single-crystal zircon (U-Th)/He (ZHe) dates versus effective uranium (eU) content from samples analyzed in [94]. Dashed orange lines next to ZHe data correspond to the modeled age distribution of ZHe dates versus eU content for crystals with an equivalent radius of 50  $\mu\text{m}$  for the main T-t trajectory (larger diagram), with gradual tonalities indicating different maximum temperatures simulated. (D) Single-crystal Raman-based radiation damage ages versus measured zircon (U-Th)/He dates. Radiation damage ages were calculated following [93]. Symbols are color coded according to the eU content of the analyzed crystal. The dashed gray line represents a one-to-one correlation between the methods. Modified from [94].

The oldest ZHe dates are less than 100 Myr younger than the late stages of the Neoproterozoic Pan-African/Brasiliano orogenic cycle from which the sampled units originated [94,127–130]. They indicate that the region had already been exhumated to temperatures at least within the zircon He-PRZ by the early Paleozoic. These temperature conditions also inhibited annealing of radiation damage to the crystalline lattice of zircon, leading to long-term damage accumulation that ultimately controlled the retentivity of He in the crystals [18–20,35,131]. This is demonstrated by the strong correlation between the apparent ZHe ages and the corresponding effective uranium content in single crystals (Figure 9C). The large spread in the ZHe dates can thus be explained by the partial reset of the (U-Th)/He isotopic system after a protracted prolonged period of radiation damage accumulation.

A possible cause for this partial reset is provided by the onset of magmatism that culminated with the extrusion of the Paraná-Etendeka Large Igneous Province (LIP) in the Cretaceous (ca. 134 Ma, [132,133]), the second largest magmatic province in the world. In the study area, this event is best recorded by the emplacement of numerous intrusions associated with the Florianópolis Dyke Swarm, an important feeding dyke system of the LIP [134]. The recurrent intrusion of basaltic dykes during the course of the magmatic event is likely to have had a more lasting impact on the local geothermal gradient than that of the extrusive flood volcanism. Forward modeling was performed for correlation with the ZHe-eU data using the zircon radiation damage accumulation and annealing model (ZRDAAM [35]), which is able to account for much of the distribution observed in the dataset by simulating a short-lived (<10 Myr) thermal pulse at temperatures between 180° and 220 °C (Figure 9C). A similar pattern could also be reconstructed by simulating protracted exposure to temperature conditions using forward modeling to reproduce the zircon data. However, this scenario alone is less likely, as Devonian sediments situated less than 10 km to the west of the studied area indicate a near-surface exposure at some point in the Paleozoic. Considering that the samples were collected along three transects separated by some tens of kilometers, a combination of both processes (long-term exposure to temperature conditions within the zircon He-PRZ and rapid magmatism-induced heating) may have led to the observed dispersion. The modeling of the ZHe data also highlighted limitations of the ZRDAAM when it comes to predicting ZHe dates in crystals that have been subjected to very high doses of radiation damage, as pointed out in other studies (e.g., [19]). In this case, U-Th zonation most likely plays an important role in controlling He retentivity, as low-eU zones may create He pockets even in highly damaged crystals [72]. The final exhumation of the study area, constrained at ca. 75 to 55 Ma by the AHe data, is probably linked to the erosion of the volcanic cover during the post-rift uplift of the passive margin.

Another interesting aspect of the work of Hueck et al. [94] is the application of Raman spectroscopy for investigating characteristics of the crystals analyzed for (U-Th)/He. Indeed, Raman spectroscopy provides an estimation of alpha radiation damage in zircon crystals [52,53] which, together with eU data, can be used to model simplified radiation damage ages [91,93]. With the exception of a few outlying results, the radiation damage ages calculated by Hueck et al. [94] have a range that is comparable to the ZHe dates (Figure 9D), in agreement with the interpretation that the zircon crystals have accumulated radiation damage since at least the early Paleozoic. The radiation damage ages also have a remarkable spread that mirrors that of the ZHe dates, though they are consistently older. These observations suggest that the analyzed zircon crystals also experienced partial annealing under temperature conditions similar to those of the ZHe PRZ, though the consistently older ages (in comparison to the ZHe results) are in disagreement with most estimates that the temperatures necessary for significant zircon annealing are higher than for widespread He diffusion ([92] and references therein). In addition, the calculated ages correlate with eU, showing evidence that crystals with varying damage densities were subjected to different annealing mechanisms or rates. In any case, the study of Hueck et al. [94] demonstrates that the use of Raman spectroscopy can provide valuable, additional information for the

interpretation of (U-Th)/He data. New approaches, such as high-resolution mapping of crystals (e.g., [135]), may help constrain the effects of U-Th zonation on He retentivity, as mentioned above, and thus help improve currently available diffusion models.

#### 4. Recommendations

As shown in this review, the interpretation of single-grain (U-Th)/He data can be complex. Date dispersion is expected in any (U-Th)/He dataset, mostly as a result of radiation damage, which is recognized to control He diffusion within crystals. This recognition has proved to be highly valuable to constrain thermal histories through modeling of the data. At a practical level, models describe the evolution of a given instance of (U-Th)/He systems as a function of time and temperature assuming a particular starting arrangement and subsequent time–temperature history. These instances include the concentration of radiogenic  $^4\text{He}$  atoms within crystals and loss of these atoms through alpha ejection.

Here, we provide some recommendations that intend to assist in the interpretation of (U-Th)/He dates and the determination of thermal histories.

- (1) Careful selection of the crystals to be analyzed and use of adequate imaging protocols are mandatory to obtain geologically meaningful (U-Th)/He dates. Notably, these are critical steps for proper alpha ejection correction. In particular, selected grain crystals must be of a sufficient size and as euhedral as possible, especially in the case of zircon. eU-rich mineral inclusions must be identified, especially in low-eU mineral phases such as magnetite, spinel and rutile. This can be performed using optical characterization for transparent minerals, but new techniques such as CT scans [49] have the power to inspect the presence of inclusions for all types of crystals with an even better resolution.
- (2) For zircon, titanite and rutile, characterization of the degree of damage within crystals is a pre-requisite to interpret (U-Th)/He dates. Color-based selection of zircon crystals can promote considering crystals with a wide range of accumulated alpha doses [86]. In addition, Raman spectroscopy is a non-destructive and time-saving method for quantifying the amount of damage in crystals. Ultimately, analyzing crystals with different radiation damage contents helps document (U-Th)/He date–eU correlations and constrain thermal histories.
- (3) Regarding date interpretation, it must be stressed that (U-Th)/He data result from the net balance between the production, accumulation and loss of  $^4\text{He}$  atoms for a particular thermal history. We therefore recommend avoiding calculating and expressing (U-Th)/He results as mean ages, as this will remove pertinent information for the proper reconstruction of thermal histories. As presented in Figure 4, any source of date dispersion should be discussed with regard to the thermal history and geology. To do so, a first exploration of mineral phases surrounding the crystals selected for dating should be conducted to identify possible alpha implantation, especially when dealing with low-eU minerals. Analyzing dependencies of (U-Th)/He dates with the diffusion domain ( $R_s$ ) and effective uranium content (eU) must also be routinely performed. These steps are mandatory to exclude data arising from implantation or analytical problems, and to focus only on the geological significance of (U-Th)/He data.
- (4) Constraining the thermal history of a sample from (U-Th)/He data can be achieved thanks to He diffusion models that take into account both the production and annealing of damage. As research is still exploring He diffusion in certain mineral phases, it is important to review available He diffusion algorithms periodically. For zircon, additional work needs to be conducted to better assess parameters influencing He diffusion as the current damage-dependent model of diffusion cannot explain all ZHe data. In particular, the model is able to reproduce only qualitatively, not quantitatively, the range of single-grain ZHe dates and both positive and negative age–eU correlations (see examples of Figures 7 and 9). For titanite and rutile, no He radiation damage accumulation and annealing diffusion algorithms are currently available,

limiting the interpretation of the information provided by those thermochronological systems. It is therefore of uttermost importance to be critical and cautious with data interpretation, in order not to overinterpret the data.

- (5) Finally, we recommend, when possible, combining (U-Th)/He thermochronometers with lower- or higher-temperature thermochronometers to extend time–temperature spaces consistent with (U-Th)/He data, thereby refining the reconstruction of the thermal history of a sample. In particular, (U-Th)/He date–eU correlations yielded by a sample are the result of its entire thermal history and are not only shaped by the most recent cooling event. While a combination of ZHe, THe or RHe dating with AFT or AHe analysis often reveals the late thermal history of a sample, apatite, rutile or titanite U/Pb dating has proved to help constrain the earlier history of samples. Methods such as (U-Th)/He baddeleyite [27], (U-Th)/He garnet [28] or (U-Th)/He monazite [29,30,136] show good promise for new applications and should be watched closely.

**Author Contributions:** Writing—review and editing, C.G., M.H., S.T., B.H., S.S., P.S. and L.T.-G.; visualization, C.G., M.H., S.T., B.H. and S.S.; supervision, C.G.; project administration, C.G. All authors have read and agreed to the published version of the manuscript.

**Funding:** This research on He diffusion in minerals was funded thanks to the Agence National de la Recherche grants ANR-06-JCJC-0079 and ANR-12-NS06-0005-01 (HeDiff projects). M. Hueck thanks FAPESP for a post-doctoral fellowship (grant 2019/06838-2), B. Heller’ doctoral fellowship is funded by the ANR RECA project (ANR-17-CE01-0012) and S. Ternois’ post-doctoral fellowship is funded by the LabEx VOLTAIRE (LABX-100-01) project.

**Data Availability Statement:** This is a review, and therefore all data can be found indexed from the original sources in the citations that are provided.

**Acknowledgments:** The two anonymous reviewers and the editor are warmly thanked for their constructive suggestions.

**Conflicts of Interest:** The authors declare no conflict of interest. The funders had no role in the design of the study; in the collection, analyses or interpretation of data; in the writing of the manuscript; or in the decision to publish the results.

## References

- Chew, D.M.; Spikings, R.A. Apatite U-Pb Thermochronology: A Review. *Minerals* **2021**, *11*, 1095. [[CrossRef](#)]
- Spikings, R.A.; Popov, D.V. Thermochronology of Alkali Feldspar and Muscovite at  $T > 150^{\circ}\text{C}$  Using the  $40\text{Ar}/39\text{Ar}$  Method: A Review. *Minerals* **2021**, *11*, 1025. [[CrossRef](#)]
- Zeitler, P.; Herczeg, A.; McDougall, I.; Honda, M. U-Th-He dating of apatite: A potential thermochronometer. *Geochim. Cosmochim. Acta* **1987**, *51*, 2865–2868. [[CrossRef](#)]
- Reiners, P.W.; Farley, K.A. Helium diffusion and (U-Th)/He thermochronology of titanite. *Geochim. Cosmochim. Acta* **1999**, *63*, 3845–3859. [[CrossRef](#)]
- Farley, K.A. (U-Th)/He dating: Techniques, calibrations, and applications. In *Noble Gases in Geochemistry and Cosmochemistry*; Porcelli, D.P., Ballentine, C.J., Wieler, R., Eds.; Walter de Gruyter GmbH: Berlin, Germany, 2002; pp. 819–844.
- Reiners, P.W. Zircon (U-Th)/He thermochronometry. *Rev. Mineral. Geochem.* **2005**, *58*, 151–179. [[CrossRef](#)]
- Reiners, P.W.; Brandon, M.T. Using thermochronology to understand orogenic erosion. *Annu. Rev. Earth Planet. Sci.* **2006**, *34*, 419–466. [[CrossRef](#)]
- Ternois, S.; Odlum, M.; Ford, M.; Pik, R.; Stockli, D.; Tibari, B.; Vacherat, A.; Bernard, V. Thermochronological Evidence of Early Orogenesis, Eastern Pyrenees, France. *Tectonics* **2019**, *38*, 1308–1336. [[CrossRef](#)]
- Tremblay, M.M.; Fox, M.; Schmidt, J.L.; Tripathy-Lang, A.; Wielicki, M.M.; Harrison, T.M.; Zeitler, P.K.; Shuster, D.L. Erosion in southern Tibet shut down at  $\sim 10$  Ma due to enhanced rock uplift within the Himalaya. *Proc. Natl. Acad. Sci. USA* **2015**, *112*, 12030–12035. [[CrossRef](#)]
- Gallagher, K.; Brown, R.; Johnson, C. Fission track analysis and its applications to geological problems. *Annu. Rev. Earth Planet. Sci.* **1998**, *26*, 519–572. [[CrossRef](#)]
- Bernet, M. A field-based estimate of the zircon fission-track closure temperature. *Chem. Geol.* **2009**, *259*, 181–189. [[CrossRef](#)]
- Ehlers, T.A. Crustal Thermal Processes and the Interpretation of Thermochronometer Data. *Rev. Miner. Geochem.* **2005**, *58*, 315–350. [[CrossRef](#)]

13. Braun, J.; van der Beek, P.; Batt, G. *Quantitative Thermochronology: Numerical Methods for the Interpretation of Thermochronological Data*; Cambridge University Press: Cambridge, MA, USA, 2006; p. 258.
14. Ault, A.K.; Gautheron, C.; King, G.E. Innovations in (U-Th)/He, fission-track, and trapped-charge thermochronometry with applications to earthquakes, weathering, surface-mantle connections, and the growth and decay of mountains. *Tectonics* **2019**, *38*, 3705–3739. [[CrossRef](#)]
15. Ehlers, T.A.; Farley, K.A. Apatite (U+Th)/He thermochronometry: Methods and applications to problems in tectonic and surface processes. *Earth Planet. Sci. Lett.* **2003**, *206*, 1–14. [[CrossRef](#)]
16. Baughman, J.S.; Flowers, R.M.; Metcalf, J.R.; Dhansay, T. Influence of radiation damage on titanite diffusion kinetics. *Geochim. Cosmochim. Acta* **2017**, *205*, 50–64. [[CrossRef](#)]
17. Flowers, R. Exploiting radiation damage control on apatite (U-Th)/He dates in cratonic regions. *Earth Planet. Sci. Lett.* **2009**, *277*, 148–155. [[CrossRef](#)]
18. Guenther, W.R.; Reiners, P.W.; Drake, H.; Tilberg, M. Zircon, titanite, and apatite (U-Th)/He ages and age-eU correlations from the Fennoscandian Shield, southern Sweden. *Tectonics* **2017**, *36*, 1254–1274. [[CrossRef](#)]
19. Johnson, J.E.; Flowers, R.M.; Baird, G.B.; Maham, K.M. “Inverted” zircon and apatite (U-Th)/He dates from the Front Range, Colorado: High-damage zircon as a low-temperature (< 50 °C) thermochronometer. *Earth Planet. Sci. Lett.* **2017**, *466*, 80–90. [[CrossRef](#)]
20. Orme, D.A.; Guenther, W.R.; Laskowski, A.K.; Reiners, P.W. Long-term tectonothermal history of Laramide basement from zircon–He age-eU correlations. *Earth Planet. Sci. Lett.* **2016**, *453*, 119–130. [[CrossRef](#)]
21. Robinson, K.H.; Flowers, R.; Metcalf, J.R. Rutile (U-Th)/He Thermochronology: Temperature Sensitivity and Radiation Damage Effects. *Geochem. Geophys. Geosyst.* **2019**, *20*, 4737–4755. [[CrossRef](#)]
22. Blackburn, T.J.; Stockli, D.F.; Walker, J.D. Magnetite (U-Th)/He dating and its application to the geochronology of intermediate to mafic volcanic rocks. *Earth Planet. Sci. Lett.* **2007**, *259*, 360–371. [[CrossRef](#)]
23. Cooperdock, E.H.; Stockli, D.F. Dating exhumed peridotite with spinel (U-Th)/He chronometry. *Earth Planet. Sci. Lett.* **2018**, *489*, 219–227. [[CrossRef](#)]
24. Cooperdock, E.H.; Stockli, D.F. Unraveling alteration histories in serpentinites and associated ultramafic rocks with magnetite (U-Th)/He geochronology. *Geology* **2016**, *44*, 967–970. [[CrossRef](#)]
25. Schwartz, S.; Gautheron, C.; Ketcham, R.A.; Brunet, F.; Corre, M.; Agranier, A.; Pinna Jamme, R.; Haurine, F.; Monvoisin, G.; Riel, N. Unraveling the exhumation history of high-pressure ophiolites using magnetite (U-Th-Sm)/He thermochronometry. *Earth Planet. Sci. Lett.* **2020**, *543*, 116359. [[CrossRef](#)]
26. Stanley, J.R.; Flowers, R.M. Dating kimberlite emplacement with zircon and perovskite (U-Th)/He geochronology. *Geochem. Geophys. Geosyst.* **2016**, *17*, 4517–4533. [[CrossRef](#)]
27. Metcalf, J.R.; Flowers, R.M. Initial development of baddeleyite (U-Th)/He thermochronology. In *Geological Society of America Abstracts with Programs, Proceedings of the 125th Anniversary Annual Meeting and Expo, Denver, CO, USA, 27–30 October 2013*; The Geological Society of America: Denver, CO, USA, 2013.
28. Seman, S.; Stockli, D.F.; Smye, A.J.; Hernandez Goldstein, E.J. Garnet (U-Th)/He thermochronometry and its application to exhumed high-pressure low-temperature metamorphic rocks. In *Proceedings of the Thermo 2014: 14th International Conference on Thermochronology, Chamonix, France, 8–12 September 2014*.
29. Boyce, J.W.; Hodges, K.V.; Olszewski, W.J.; Jercinovic, M.J. He diffusion in monazite: Implications for (U-Th)/He thermochronology. *Geochem. Geophys. Geosyst.* **2005**, *6*, 1–12. [[CrossRef](#)]
30. Farley, K.A.; Stockli, D.F. (U-Th)/He Dating of Phosphates: Apatite, Monazite, and Xenotime. *Rev. Mineral. Geochem.* **2002**, *48*, 559–577. [[CrossRef](#)]
31. Peterman, E.M.; Hourigan, J.K.; Grove, M. Experimental and geologic evaluation of monazite (U-Th)/He thermochronometry: Catnip Sill, Catalina Core Complex, Tucson, AZ. *Earth Planet. Sci. Lett.* **2014**, *403*, 48–55. [[CrossRef](#)]
32. Farley, K. Helium diffusion from apatite: General behavior as illustrated by Durango fluorapatite. *J. Geophys. Res. Earth Surf.* **2000**, *105*, 2903–2914. [[CrossRef](#)]
33. Shuster, D.L.; Flowers, R.M.; Farley, K.A. The influence of natural radiation damage on helium diffusion kinetics in apatite. *Earth Planet. Sci. Lett.* **2006**, *249*, 148–161. [[CrossRef](#)]
34. Gerin, C.; Gautheron, C.; Oliviero, E.; Bachelet, C.; Djimbi, D.M.; Seydoux-Guillaume, A.-M.; Tassan-Got, L.; Sarda, P.; Roques, J.; Garrido, F. Influence of vacancy damage on He diffusion in apatite, investigated at atomic to mineralogical scales. *Geochim. Cosmochim. Acta* **2017**, *197*, 87–103. [[CrossRef](#)]
35. Guenther, W.; Reiners, P.W.; Ketcham, R.; Nasdala, L.; Giester, G. Helium diffusion in natural zircon: Radiation damage, anisotropy, and the interpretation of zircon (U-Th)/He thermochronology. *Am. J. Sci.* **2013**, *313*, 145–198. [[CrossRef](#)]
36. Ziegler, J.F. *Helium Stopping Powers and Ranges in All Elements*; Pergamon Press: London, UK, 1977.
37. Biersack, J.P.; Ziegler, J.F. The Stopping and Range of Ions in Solids. In *Ion Implantation Techniques*; Ryssel, H., Glawischnig, H., Eds.; Springer Series in Electrophysics; Springer: Berlin/Heidelberg, Germany, 1982; Volume 10. [[CrossRef](#)]
38. Farley, K.A.; Wolf, R.A.; Silver, L.T. The effects of long alpha-stopping on (U-Th)/He ages. *Geochim. Cosmochim. Acta* **1996**, *21*, 4223–4229. [[CrossRef](#)]
39. Ketcham, R.A.; Gautheron, C.; Tassan-Got, L. Accounting for long alpha-particle stopping distances in (U-Th-Sm)/He geochronology: Refinement of the baseline case. *Geochim. Cosmochim. Acta* **2011**, *75*, 7779–7791. [[CrossRef](#)]

40. Gautheron, C.; Tassan-Got, L.; Ketcham, R.A.; Dobson, K.J. Accounting for long alpha-particle stopping distances in (U-Th-Sm)/He geochronology: 3D modeling of diffusion, zoning, implantation, and abrasion. *Geochimica Cosmochimica Acta* **2012**, *96*, 44–56. [[CrossRef](#)]
41. Hourigan, J.K.; Reiners, P.W.; Brandon, M.T. U-Th zonation-dependent alpha-ejection in (U-Th)/He chronometry. *Geochim. Cosmochim. Acta* **2005**, *69*, 3349–3365. [[CrossRef](#)]
42. Meesters, A.G.C.A.; Dunai, T.J. Solving the production-diffusion equation for finite diffusion domains of various shapes Part II. Application to cases with alpha-ejection and nonhomogeneous distribution of the source. *Chem. Geol.* **2002**, *186*, 347–363. [[CrossRef](#)]
43. Stockli, D.; Farley, K.A. Empirical constraints on the titanite (U-Th)/He partial retention zone from the KTB drill hole. *Chem. Geol.* **2004**, *207*, 223–236. [[CrossRef](#)]
44. Flowers, R.; Zeitler, P.K.; Danišik, M.; Reiners, P.W.; Gautheron, C.; Ketcham, R.A.; Metcalf, J.R.; Stockli, D.; Enkelmann, E.; Brown, R.W. (U-Th)/He chronology: Part 1. Data, uncertainty, and reporting. *GSA Bull.* **2022**. [[CrossRef](#)]
45. Ewing, R.; Weber, W.; Clinard, F. Radiation effects in nuclear waste forms for high-level radioactive waste. *Prog. Nucl. Energy* **1995**, *29*, 63–127. [[CrossRef](#)]
46. Ríos, S.; Salje, E.; Zhang, M.; Ewing, R.C. Amorphization in zircon: Evidence for direct impact damage. *J. Phys. Condens. Matter* **2000**, *12*, 2401–2412. [[CrossRef](#)]
47. Fleischer, R.; Price, P. Techniques for geological dating of minerals by chemical etching of fission fragment tracks. *Geochim. Cosmochim. Acta* **1964**, *28*, 1705–1714. [[CrossRef](#)]
48. Tagami, T. Zircon Fission-Track Thermochronology and Applications to Fault Studies. *Rev. Miner. Geochem.* **2005**, *58*, 95–122. [[CrossRef](#)]
49. Cooperdock, E.H.; Ketcham, R.A.; Stockli, D.F. Resolving the effects of 2D versus 3D grain measurements on (U-Th)/He age data and reproducibility. *Geochronology* **2019**, *1*, 17–41. [[CrossRef](#)]
50. Gastil, R.G.; Delisle, M.; Morgan, J. Some Effects of Progressive Metamorphism on Zircons. *GSA Bull.* **1967**, *78*, 879–906. [[CrossRef](#)]
51. Gautheron, C.; Djimbi, D.M.; Roques, J.; Balout, H.; Ketcham, R.A.; Simoni, E.; Pik, R.; Seydoux-Guillaume, A.-M.; Tassan-Got, L. A multi-method, multi-scale theoretical study of He and Ne diffusion in zircon. *Geochim. Cosmochim. Acta* **2020**, *268*, 348–367. [[CrossRef](#)]
52. Nasdala, L.; Wenzel, M.; Vavra, G.; Irmer, G.; Wenzel, T.; Kober, B. Metamictisation of natural zircon: Accumulation versus thermal annealing of radioactivity-induced damage. *Contrib. Miner. Pet.* **2001**, *141*, 125–144. [[CrossRef](#)]
53. Palenik, C.S.; Nasdala, L.; Ewing, R.C. Radiation damage in zircon. *Am. Miner.* **2003**, *88*, 770–781. [[CrossRef](#)]
54. Beirau, T.; Bismayer, U.; Mihailova, B.; Paulmann, C.; Groat, L. Structural phenomena of metamict titanite: A synchrotron, X-ray diffraction and vibrational spectroscopic study. *Phase Transit.* **2010**, *83*, 694–702. [[CrossRef](#)]
55. Zhang, M.; Salje, E.; Redfern, S.; Bismayer, U.; A Groat, L. Intermediate structures in radiation damaged titanite (CaTiSiO<sub>5</sub>): A Raman spectroscopic study. *J. Phys. Condens. Matter* **2013**, *25*, 115402. [[CrossRef](#)]
56. Djimbi, D.M.; Gautheron, C.; Roques, J.; Tassan-Got, L.; Gerin, C.; Simoni, E. Impact of apatite chemical composition on (U-Th)/He thermochronometry: An atomistic point of view. *Geochim. Cosmochim. Acta* **2015**, *167*, 162–176. [[CrossRef](#)]
57. Gautheron, C.; Tassan-Got, L. A Monte Carlo approach to diffusion applied to noble gas/helium thermochronology. *Chem. Geol.* **2010**, *273*, 212–224. [[CrossRef](#)]
58. Meesters, A.G.C.A.; Dunai, T.J. Solving the production-diffusion equation for finite diffusion domains of various shapes Part I. Implications from low-temperature (U-Th)/He thermochronology. *Chem. Geol.* **2002**, *186*, 333–344. [[CrossRef](#)]
59. McDannell, K.; Zeitler, P.K.; Janes, D.G.; Idelman, B.D.; Fayon, A.K. Screening apatites for (U-Th)/He thermochronometry via continuous ramped heating: He age components and implications for age dispersion. *Geochim. Cosmochim. Acta* **2018**, *223*, 90–106. [[CrossRef](#)]
60. Devanathan, R.; Corrales, L.R.; Weber, W.J.; Chartier, A.; Meis, C. Molecular dynamics simulation of energetic uranium recoil damage in zircon. *Mol. Simul.* **2006**, *32*, 1069–1077. [[CrossRef](#)]
61. Bassal, F.; Roques, J.; Corre, M.; Ketcham, R.A.; Brunet, F.; Schwartz, S.; Pinna Jamme, R.; Tassan-Got, L.; Gautheron, C. He diffusion in magnetite: Combining theoretical multi-scale and experimental studies. *Submitt. Miner.* **2022**, *in press*.
62. Ketcham, R.; Guenther, W.R.; Reiners, P.W. Geometric analysis of radiation damage connectivity in zircon, and its implications for helium diffusion. *Am. Miner.* **2013**, *98*, 350–360. [[CrossRef](#)]
63. Dodson, M.H. Closure temperature in cooling geochronological and petrological systems. *Contrib. Miner. Pet.* **1973**, *40*, 259–274. [[CrossRef](#)]
64. Gautheron, C.; Zeitler, P.K. Noble Gases Deliver Cool Dates from Hot Rocks. *Elements* **2020**, *16*, 303–309. [[CrossRef](#)]
65. Wolf, R.; Farley, K.A.; Kass, D. A sensitivity analysis of the apatite (U-Th)/He thermochronometer. *Chem. Geol.* **1998**, *148*, 105–114. [[CrossRef](#)]
66. Cherniak, D.; Watson, E. Helium diffusion in rutile and titanite, and consideration of the origin and implications of diffusional anisotropy. *Chem. Geol.* **2011**, *288*, 149–161. [[CrossRef](#)]
67. House, M.A.; Farley, K.A.; Stockli, D. Helium chronometry of apatite and titanite Nd-YAG laser heating. *Earth Planet. Sci. Lett.* **2000**, *183*, 365–368. [[CrossRef](#)]
68. Gérard, B.; Robert, X.; Gautheron, C.; Grujic, D.; Audin, L.; Bernet, M.; Balvay, M. Zircon (U-Th)/He closure temperature lower than apatite thermochronometric systems: Reconciliation of a paradox. *Minerals* **2022**, *12*, 145. [[CrossRef](#)]

69. Guenther, W.R. Implementation of an Alpha Damage Annealing Model for Zircon (U-Th)/He Thermochronology With Comparison to a Zircon Fission Track Annealing Model. *Geochem. Geophys. Geosyst.* **2020**, *22*, e2019GC008757. [[CrossRef](#)]
70. Stockli, D.; Wolfe, M.R.; Blackburn, T.J.; Zack, T.; Walker, J.D.; Luvizotto, G.L. He diffusion and (U-Th)/He thermochronometry of rutile. In *American Geophysical Union, Fall Meeting*; American Geophysical Union: Washington, DC, USA, 2007; Volume 2007, pp. V23C–1548.
71. Heller, B.M.; Lünsdorf, N.K.; Dunkl, I.; Molnár, F.; Von Eynatten, H. Estimation of radiation damage in titanites using Raman spectroscopy. *Am. Miner.* **2019**, *104*, 857–868. [[CrossRef](#)]
72. Danišik, M.; McInnes, B.I.A.; Kirkland, C.L.; McDonald, B.J.; Evans, N.J.; Becker, T. Seeing is believing: Visualization of He distribution in zircon and implications for thermal history reconstruction on single crystals. *Sci. Adv.* **2017**, *3*, e1601121. [[CrossRef](#)]
73. Glotzbach, C.; Lang, K.A.; Avdievitch, N.N.; Ehlers, T. Increasing the accuracy of (U-Th(-Sm))/He dating with 3D grain modelling. *Chem. Geol.* **2019**, *506*, 113–125. [[CrossRef](#)]
74. Herman, F.; Braun, J.; Senden, T.J.; Dunlap, W.J. (U-Th)/He chronometry: Mapping 3D geometry using micro-X-ray tomography and solving the associated production-diffusion equation. *Chem. Geol.* **2007**, *242*, 126–136. [[CrossRef](#)]
75. Guenther, W.R.; Reiners, P.W.; Chowdhury, U. Isotope dilution analysis of Ca and Zr in apatite and zircon (U-Th)/He chronometry. *Geochem. Geophys. Geosyst.* **2016**, *17*, 1623–1640. [[CrossRef](#)]
76. Reiners, P.W.; Nicolescu, S. Measurement of parent nuclides for (U-Th)/He chronometry by solution sector ICP-MS. *ARHDL Rep.* **2007**, *1*, 1–33.
77. Gautheron, C.; Pinna-Jamme, R.; Derycke, A.; Ahadi, F.; Sanchez, C.; Haurine, F.; Monvoisin, G.; Barbosa, D.; Delpech, G.; Maltese, J.; et al. Technical note: Analytical protocols and performance for apatite and zircon (U-Th)/He analysis on quadrupole and magnetic sector mass spectrometer systems between 2007 and 2020. *Geochronology* **2021**, *3*, 351–370. [[CrossRef](#)]
78. Boyce, J.W.; Hodges, K.V.; Olszewski, W.J.; Jercinovic, M.J.; Carpenter, B.D.; Reiners, P.W. Laser microprobe (U-Th)/He geochronology. *Geochim. Cosmochim. Acta* **2006**, *70*, 3031–3039. [[CrossRef](#)]
79. Evans, N.J.; Wilson, N.S.F.; Cline, J.S.; McInnes, B.I.A.; Byrne, J. Fluorite (U-Th)/He thermochronology: Constraints on the low temperature history of the Yucca Mountain, Nevada. *Appl. Geochem.* **2005**, *20*, 1099–1105. [[CrossRef](#)]
80. Hacker, B.R.; Kelemen, P.B.; Rioux, M.; McWilliams, M.O.; Gans, P.B.; Reiners, P.W.; Layer, P.W.; Söderlund, U.; Vervoort, J.D. Thermochronology of the Talkeetna intraoceanic arc of Alaska: Ar/Ar, U-Th/He, Sm-Nd, and Lu-Hf dating. *Tectonics* **2011**, *30*. [[CrossRef](#)]
81. Reiners, P.W.; Campbell, I.H.; Nicolescu, S.; Allen, C.M.; Hourigan, J.K.; Garver, J.I.; Mattinson, J.M.; Cowan, D.S. (U-Th)/(He-Pb) double dating of detrital zircons. *Am. J. Sci.* **2005**, *305*, 259–311. [[CrossRef](#)]
82. Dobson, K.J.; Stuart, F.M.; Dempster, T.J. U and Th zonation in Fish Canyon Tuff zircons: Implications for a zircon (U-Th)/He standard. *Geochim. Cosmochim. Acta* **2008**, *72*, 4745–4755. [[CrossRef](#)]
83. Kraml, M.; Pik, R.; Rahn, M.; Selbekk, R.; Carignan, J.; Keller, J. A new multi-mineral age reference material for <sup>40</sup>Ar/<sup>39</sup>Ar, (U-Th)/He and fission track dating methods: The Limberg t3 tuff. *Geostand. Geoanal. Res.* **2006**, *30*, 73–86. [[CrossRef](#)]
84. Schmitz, M.D.; Bowering, S.A. U-Pb zircon and titanite systematics of the Fish Canyon Tuff: An assessment of high-precision U-Pb geochronology and its application to young volcanic rocks. *Geochim. Cosmochim. Acta* **2001**, *65*, 2571–2587. [[CrossRef](#)]
85. Vermeesch, P. HelioPlot, and the treatment of overdispersed (U-Th-Sm)/He data. *Chem. Geol.* **2010**, *271*, 108–111. [[CrossRef](#)]
86. Ault, A.K.; Guenther, W.R.; Moser, A.C.; Miller, G.H.; Refsnider, K.A. Zircon grain selection reveals (de)coupled metamictization, radiation damage, and He diffusivity. *Chem. Geol.* **2018**, *490*, 1–12. [[CrossRef](#)]
87. Zhang, M.; Salje, E.; Farnan, I.; Graeme-Barber, A.; Daniel, P.; Ewing, R.C.; Clark, A.M.; Leroux, H. Metamictization of zircon: Raman spectroscopic study. *J. Phys. Condens. Matter* **2000**, *12*, 1915–1925. [[CrossRef](#)]
88. Beirau, T.; Mihailova, B.; Matveeva, G.; Kolb, U.; Malcherek, T.; Groat, L.A.; Bismayer, U. Structural anisotropy and annealing-induced nanoscale atomic rearrangements in metamict titanite. *Am. Miner.* **2012**, *97*, 1354–1365. [[CrossRef](#)]
89. Zhang, M.; Salje, E.K. Spectroscopic Characterization of Metamictization and Recrystallization in Zircon and Titanite. *Phase Transitions* **2003**, *76*, 117–136. [[CrossRef](#)]
90. Váczi, T.; Nasdala, L. Electron-beam-induced annealing of natural zircon: A Raman spectroscopic study. *Phys. Chem. Miner.* **2017**, *44*, 389–401. [[CrossRef](#)]
91. Härtel, B.; Jonckheere, R.; Wauschkuhn, B.; Hofmann, M.; Frölich, S.; Ratschbacher, L. Zircon Raman dating: Age equation and calibration. *Chem. Geol.* **2021**, *579*, 120351. [[CrossRef](#)]
92. Härtel, B.; Jonckheere, R.; Wauschkuhn, B.; Ratschbacher, L. The closure temperature(s) of zircon Raman dating. *Geochronology* **2021**, *3*, 259–272. [[CrossRef](#)]
93. Pidgeon, R. Zircon radiation damage ages. *Chem. Geol.* **2014**, *367*, 13–22. [[CrossRef](#)]
94. Hueck, M.; Dunkl, I.; Heller, B.; Basei, M.A.S.; Siegesmund, S. (U-Th)/He Thermochronology and Zircon Radiation Damage in the South American Passive Margin: Thermal Overprint of the Paraná LIP? *Tectonics* **2018**, *37*, 4068–4085. [[CrossRef](#)]
95. Spiegel, C.; Kohn, B.; Belton, D.; Berner, Z.; Gleadow, A. Apatite (U-Th-Sm)/He thermochronology of rapidly cooled samples: The effect of He implantation. *Earth Planet. Sci. Lett.* **2009**, *285*, 105–114. [[CrossRef](#)]
96. Schwartz, S.; Lardeaux, J.M.; Tricart, P.; Guillot, S.; Labrin, E. Diachronous exhumation of HP?LT metamorphic rocks from south-western Alps: Evidence from fission-track analysis. *Terra Nova* **2007**, *19*, 133–140. [[CrossRef](#)]
97. Ketcham, R.A. Forward and inverse modelling of low-temperature thermochronology data. *Rev. Mineral. Geochem.* **2005**, *58*, 275–314. [[CrossRef](#)]

98. Gallagher, K. Transdimensional inverse thermal history modeling for quantitative thermochronology. *J. Geophys. Res. Earth Surf.* **2012**, *117*, 16. [[CrossRef](#)]
99. Braun, J. Pecube: A new finite element code to solve the heat transport equation in three dimensions in the Earth's crust including the effects of a time-varying, finite amplitude surface topography. *Comput. Geosci.* **2003**, *29*, 787–794. [[CrossRef](#)]
100. Ginster, U.; Reiners, P.W.; Nasdala, L.; Chanmuang, C. Annealing kinetics of radiation damage in zircon. *Geochim. Cosmochim. Acta* **2019**, *249*, 225–246. [[CrossRef](#)]
101. Odlum, M.L.; Stockli, D.F. Thermotectonic Evolution of the North Pyrenean Agly Massif During Early Cretaceous Hyperextension Using Multi-mineral U-Pb Thermochronometry. *Tectonics* **2019**, *38*, 1509–1531. [[CrossRef](#)]
102. Yelland, A. Fission track thermotectonics of the Iberian-Eurasian plate collection. Ph.D. Thesis, Birkbeck University of London, London, UK, 1991.
103. Gunnell, Y.; Calvet, M.; Brichau, S.; Carter, A.; Aguilar, J.-P.; Zeyen, H. Low long-term erosion rates in high-energy mountain belts: Insights from thermo- and biochronology in the Eastern Pyrenees. *Earth Planet. Sci. Lett.* **2009**, *278*, 208–218. [[CrossRef](#)]
104. Golberg, J.-M.; Maluski, H. Données nouvelles et mise au point sur l'âge du métamorphisme pyrénéen. *Comptes Rendus De L'académie Des Sci.* **1988**, *306*, 429–435.
105. Poujol, M.; Boulvais, P.; Kosler, J. Regional-scale Cretaceous albitization in the Pyrenees: Evidence from in situ U–Th–Pb dating of monazite, titanite and zircon. *J. Geol. Soc.* **2010**, *167*, 751–767. [[CrossRef](#)]
106. Debroas, E.J. Le flysch noir albo-cenomanien témoin de la structuration albienne à senonienne de la Zone nord-pyréenne en Bigorre (Hautes-Pyrénées, France). *Bull. Société Géologique Fr.* **1990**, *6*, 273–285. [[CrossRef](#)]
107. Debroas, E.J.; Debroas, E.J. Modèle de bassin triangulaire à l'intersection de décrochements divergents pour le fosse albo-cenomanien de la Ballongue (zone nord-pyréenne, France). *Bull. Société Géologique Fr.* **1987**, *3*, 887–898. [[CrossRef](#)]
108. Ford, M.; Hemmer, L.; Vacherat, A.; Gallagher, K.; Christophoul, F. Retro-wedge foreland basin evolution along the ECORS line, eastern Pyrenees, France. *J. Geol. Soc.* **2016**, *173*, 419–437. [[CrossRef](#)]
109. Waldner, M.; Bellahsen, N.; Mouthereau, F.; Bernet, M.; Pik, R.; Rosenberg, C.L.; Balvay, M. Central Pyrenees Mountain Building: Constraints From New LT Thermochronological Data From the Axial Zone. *Tectonics* **2021**, *40*, e2020TC006614. [[CrossRef](#)]
110. Tricart, P.; Schwartz, S. A north-south section across the Queyras Schistes lustrés (Piedmont zone, Western Alps): Syn-collision refolding of a subduction wedge. *Eclogae Geol. Helv.* **2006**, *99*, 429–442. [[CrossRef](#)]
111. Schwartz, S.; Guillot, S.; Reynard, B.; Lafay, R.; Debret, B.; Nicollet, C.; Lanari, P.; Auzende, A.L. Pressure–temperature estimates of the lizardite/antigorite transition in high pressure serpentinites. *Lithosphere* **2013**, *178*, 197–210. [[CrossRef](#)]
112. Agard, P.; Monie, P.; Jolivet, L.; Goffe, B. Exhumation of the Schistes Lustres complex: In situ laser probe  $^{40}\text{Ar}/^{39}\text{Ar}$  constraints and implications for the Western Alps. *J. Metamorph. Geol.* **2002**, *20*, 599–618. [[CrossRef](#)]
113. Guenther, W.R.; Reiners, P.W.; DeCelles, P.G.; Kendall, J. Sevier belt exhumation in central Utah constrained from complex zircon (U-Th)/He data sets: Radiation damage and He inheritance effects on partially reset detrital zircons. *Geol. Soc. Am. Bull.* **2015**, *127*, 323–348. [[CrossRef](#)]
114. Baughman, J.S.; Flowers, R.M. Deciphering a 2 Gyr-Long Thermal History From a Multichronometer (U-Th)/He Study of the Phalaborwa Carbonatite, Kaapvaal Craton, South Africa. *Geochem. Geophys. Geosyst.* **2018**, *19*, 1581–1594. [[CrossRef](#)]
115. DeLucia, M.S.; Guenther, W.R.; Marshak, S.; Thomson, S.N.; Ault, A.K. Thermochronology links denudation of the Great Unconformity surface to the supercontinent cycle and snowball Earth. *Geology* **2018**, *46*, 167–170. [[CrossRef](#)]
116. Dobson, K.J.; Persano, C.; Stuart, F. Quantitative constraints on mid- to shallow-crustal processes using the zircon (U-Th)/He thermochronometer. *Geol. Soc. Lond.* **2009**, *324*, 47–56. [[CrossRef](#)]
117. Ksienzyk, A.K.; Dunkl, I.; Jacobs, J.; Fossen, H.; Kohlmann, F. From orogen to passive margin: Constraints from fission track and (U-Th)/He analyses on Mesozoic uplift and fault reactivation in SW Norway. In *New Perspectives on the Caledonides of Scandinavia and Related Areas*; Corfu, F., Gasser, D., Chew, D.M., Eds.; The Geological Society of London: London, UK, 2014.
118. Hueck, M.; Dunkl, I.; Oriolo, S.; Wemmer, K.; Basei, M.A.; Siegesmund, S. Comparing contiguous high- and low-elevation continental margins: New (U-Th)/He constraints from South Brazil and an integration of the thermochronological record of the southeastern passive margin of South America. *Tectonophysics* **2019**, *770*, 228222. [[CrossRef](#)]
119. Cogné, N.; Gallagher, K.; Cobbold, P.R.; Riccomini, C.; Gautheron, C. Post-breakup tectonics in southeast Brazil from thermochronological data and combined inverse-forward thermal history modeling. *J. Geophys. Res. Earth Surf.* **2012**, *117*, 1117–11413. [[CrossRef](#)]
120. Gallagher, K.; Hawkesworth, C.J.; Mantovani, M.S.M. The denudation history of the onshore continental margin of SE Brazil inferred from apatite fission track data. *J. Geophys. Res. Earth Surf.* **1994**, *99*, 18117–18145. [[CrossRef](#)]
121. Hackspacher, P.; Ribeiro, L.; Ribeiro, M.; Fetter, A.; Neto, J.H.; Tello, C.; Dantas, E. Consolidation and Break-up of the South American Platform in Southeastern Brazil: Tectonothermal and Denudation Histories. *Gondwana Res.* **2004**, *7*, 91–101. [[CrossRef](#)]
122. Karl, M.; Glasmacher, U.A.; Kollenz, S.; Franco-Magalhaes, A.O.; Stockli, D.F.; Hackspacher, P.C. Evolution of the South Atlantic passive continental margin in southern Brazil derived from zircon and apatite (U–Th–Sm)/He and fission-track data. *Tectonophysics* **2013**, *604*, 224–244. [[CrossRef](#)]
123. Hueck, M.; Oriolo, S.; Dunkl, I.; Wemmer, K.; Oyhançabal, P.; Schanofski, M.; Basei, M.; Ângelo, S.; Siegesmund, S. Phanerozoic low-temperature evolution of the Uruguayan Shield along the South American passive margin. *J. Geol. Soc. Lond.* **2017**, *174*, 609–626. [[CrossRef](#)]



124. Machado, J.P.; Jelinek, A.R.; Bicca, M.M.; Stephenson, R.; Genezini, F.A. West Gondwana orogenies and Pangaea break-up: Thermotectonic effects on the southernmost Mantiqueira Province, Brazil. *J. Geol. Soc.* **2019**, *176*, 1056–1075. [[CrossRef](#)]
125. Machado, J.P.; Jelinek, A.R.; Stephenson, R.; Gaucher, C.; Bicca, M.M.; Chigliano, L.; Genezini, F.A. Low-temperature thermochronology of the South Atlantic margin along Uruguay and its relation to tectonic events in West Gondwana. *Tectonophysics* **2020**, *784*, 228439. [[CrossRef](#)]
126. Oliveira, C.H.E.; Jelinek, A.R.; Chemale, F., Jr.; Bernet, M. Evidence of post-Gondwana breakup in Southern Brazilian Shield: Insights from apatite and zircon fission track thermochronology. *Tectonophysics* **2016**, *666*, 173–187. [[CrossRef](#)]
127. Basei, M.A.S.; Siga, O., Jr.; Masquelin, H.; Harara, O.M.; Reis Neto, J.M.; Preciozzi, F. The Dom Feliciano Belt of Brazil and Uruguay and its Foreland Domain the Rio de la Plata Craton: Framework, tectonic evolution and correlation with similar provinces of Southwestern Africa. In *Tectonic Evolution of South America*; Cordani, U.G., Milani, E.J., Thomaz Filho, A., Campos, D.A., Eds.; Brazilian Academy of Science: Rio de Janeiro, Brazil, 2000; pp. 311–334.
128. Basei, M.; Neto, M.C.; Castro, N.; Nutman, A.; Wemmer, K.; Yamamoto, M.; Hueck, M.; Osako, L.; Siga, O.; Passarelli, C. Tectonic evolution of the Brusque Group, Dom Feliciano belt, Santa Catarina, Southern Brazil. *J. South Am. Earth Sci.* **2011**, *32*, 324–350. [[CrossRef](#)]
129. Hueck, M.; Basei, M.A.S.; Wemmer, K.; Oriolo, S.; Heidelbach, F.; Siegesmund, S. Evolution of the Major Gercino Shear Zone in the Dom Feliciano Belt, South Brazil, and implications for the assembly of southwestern Gondwana. *Int. J. Earth Sci.* **2018**, *108*, 403–425. [[CrossRef](#)]
130. Passarelli, C.R.; Basei, M.A.; Siga, O.; Mc Reath, I.; Neto, M.D.C.C. Deformation and geochronology of syntectonic granitoids emplaced in the Major Gercino Shear Zone, southeastern South America. *Gondwana Res.* **2010**, *17*, 688–703. [[CrossRef](#)]
131. Powell, J.; Schneider, D.; Stockli, D.; Fallas, K. Zircon (U-Th)/He thermochronology of Neoproterozoic strata from the Mackenzie Mountains, Canada: Implications for the Phanerozoic exhumation and deformation history of the northern Canadian Cordillera. *Tectonics* **2016**, *35*, 663–689. [[CrossRef](#)]
132. Janasi, V.A.; Freitas, V.A.; Heaman, L.H. The onset of flood basalt volcanism, Northern Paraná Basin, Brazil: A precise U–Pb baddeleyite/zircon age for a Chapecó-type dacite. *Earth Planet. Sci. Lett.* **2011**, *302*, 147–153. [[CrossRef](#)]
133. Rossetti, L.; Lima, E.F.; Waichel, B.L.; Hole, M.; Simões, M.S.; Scherer, C.M. Lithostratigraphy and volcanology of the Serra Geral Group, Paraná–Etendeka Igneous Province in Southern Brazil: Towards a formal stratigraphical framework. *J. Volcanol. Geotherm. Res.* **2018**, *355*, 98–114. [[CrossRef](#)]
134. Florisbal, L.M.; Heaman, L.M.; de Assis Janasi, V.; Bitencourt, M.F. Tectonic significance of the Florianópolis Dyke Swarm, Paraná–Etendeka Magmatic Province: A reappraisal based on precise U–Pb dating. *J. Volcanol. Geotherm. Res.* **2014**, *289*, 140–150. [[CrossRef](#)]
135. Anderson, A.J.; Hanchar, J.M.; Hodges, K.V.; van Soest, M.C. Mapping radiation damage zoning in zircon using Raman spectroscopy: Implications for zircon chronology. *Chem. Geol.* **2020**, *538*, 119494. [[CrossRef](#)]
136. Farley, K. He diffusion systematics in minerals: Evidence from synthetic monazite and zircon structure phosphates. *Geochim. Cosmochim. Acta* **2007**, *71*, 4015–4024. [[CrossRef](#)]